UC Berkeley
UC Berkeley Previously Published Works

Title
Variational Forward-Backward Charge Transfer Analysis Based on Absolutely Localized Molecular Orbitals: Energetics and Molecular Properties.

Authors
Loipersberger, Matthias
Mao, Yuezhi
Head-Gordon, Martin

Variational Forward-Backward Charge Transfer Analysis Based on Absolutely Localized Molecular Orbitals: Energetics and Molecular Properties

Matthias Loipersberger,[†,¶] Yuezhi Mao,[†,¶] and Martin Head-Gordon[*,†,‡]

†*Kenneth S. Pitzer Center for Theoretical Chemistry, Department of Chemistry, University of California, Berkeley, California 94720, USA*

‡*Chemical Sciences Division, Lawrence Berkeley National Laboratory, Berkeley, California 94720, USA*

¶*Contributed equally to this work*

E-mail: mhg@cchem.berkeley.edu

Abstract

To facilitate the understanding of charge transfer (CT) effects in dative complexes, we propose a variational forward-backward (VFB) approach to decompose the overall CT stabilization energy into contributions from forward and backward donation in the framework of energy decomposition analysis based on absolutely localized molecular orbitals (ALMO-EDA). Such a decomposition is achieved by introducing two additional constrained intermediate states in which only one direction of CT is permitted. These two "one-way" CT states are variationally relaxed such that the associated nuclear forces can be readily obtained. This allows for a facile integration into the previously developed adiabatic EDA scheme so that the molecular property changes arising from

1

forward and back donation can be separately assigned. Using ALMO-EDA augmented by this VFB model, we investigate the energetic, geometric, and vibrational features of complexes composed of CO and main group Lewis acids (BH_3, $BeO/BeCO_3$), and complexes of the N_2, CO, and BF isoelectronic series with $[Ru(II)(NH_3)_5]^{2+}$. We identify that the shift in the stretching frequency of a diatomic π-acidic ligand (XY), such as CO, results from a superposition of the shifts induced by permanent electrostatics and backward CT: permanent electrostatics can cause an either red or blue shift depending on the alignment of the XY dipole in the dative complex, and this effect becomes more pronounced with a more polar XY ligand; the back-donation to the antibonding π orbital of XY always lowers the X$-$Y bond order and thus red-shifts its stretching frequency, and the strength of this interaction decays rapidly with the intermolecular distance. We also reveal that while σ forward donation contributes significantly to energetic stabilization, it affects the vibrational feature of XY mainly by shortening the intermolecular distance, which enhances both the electrostatic interaction and backward CT but in different rates. The synergistic effect of the forward and backward donations appears to be more significant in the transition metal complexes, where the forward CT plays an essential role in overcoming the strong Pauli repulsion. These findings highlight that the shift in the XY stretching frequency is not a reliable metric for the strength of π back-donation. Overall, the VFB-augmented EDA scheme that we propose and apply in this work provides a useful tool to characterize the role played by each physical component that all together lead to the frequency shift observed.

1   Introduction

The stability of dative bonds in classical Lewis acid-base compounds is controlled by the effect of charge transfer (CT).[1] The widely used concept of donor-acceptor interaction stems from the assumption that charge flows from one fragment to another. In simple adducts like ammonia–borane or transition metal complexes with ligands that are σ-donors only (e.g. NH_3, H_2O), the assignment of the donor and acceptor moieties is straightforward, while

in many other cases, the donor and acceptor moieties interchange their roles when different orbital interactions are considered, wherein the CT is bi-directional. The relative strength of the forward and backward CT and their cooperativity impose a substantial influence on the physical and chemical properties of these donor-acceptor systems.

Complexes formed by π-acidic ligands (e.g. CO, N_2, NO, etc.) with main group or transition metal Lewis acids serve as a prominent class of examples for bi-directional CT. The synergistic effect of the σ forward donation (ligand$\rightarrow$metal) and the π back-donation (ligand$\leftarrow$metal) is a well-established concept (Dewar-Chatt-Duncanson)[2,3] and was extensively studied with various computational and analysis schemes.[4–10] The most prominent representative of this class of ligands is carbon monoxide (CO), which gives rise to the rich chemistry of a large variety of organometallic compounds ranging from mono-metal complexes (e.g. $[Ni(CO)_4]$[11]) to small multi-metal clusters (e.g. $[Fe_2(CO)_9]$[1,12,13]). Classical carbonyl compounds exhibit a red shift of 0–300 cm^{-1} in the CO stretching frequency (ν_{CO}) relative to that of the free CO molecule (2143 cm^{-1}), and the shift can be as large as 681 cm^{-1} for $Na_4[CrCO_4]$.[14] On the other hand, some other metal-carbonyl complexes (especially cationic complexes) exhibit a blue shift in ν_{CO}, which were classified as "nonclassical" metal carbonyls.[15] Besides bonding with transition metals, CO also forms adducts with main group Lewis acids where the similar bi-directional CT is observed, including various boron compounds[9,16,17] and intramolecular B/N frustrated Lewis pairs.[18] Most recently, it was shown that CO is able to form octacarbonyl complexes with alkaline earth metals (Ca, Sr, and Ba) in their zero oxidation state[19] and a strongly red-shifted cationic monocarbonyl complex with Ba^+,[20] where the ns^2 electrons are promoted to the empty $(n\text{-}1)d$ orbitals to facilitate the backbonding to CO, which further indicates the strong π-acidity of CO.

Dinitrogen (N_2), which is isoelectronic to CO, is considered to be a weaker σ-donor due to its more compact electron lone pair and also a weaker π-acceptor because of its larger HOMO-LUMO gap than CO, and consequently the coordination chemistry of N_2 is less rich. Nonetheless, since the discovery of the first complex with Ru(II),[21] many transition metal

dinitrogen complexes have been synthesized (the interested reader is referred to the published reviews[22,23]). The complexation of N_2 with transition metals is of crucial importance for artificial nitrogen fixation at ambient conditions,[24–31] which often involves the "activation" of the triple bond, i.e., the back-donation from the metal to the π^* antibonding orbital of N_2. In practice, one often measures how activated the N_2 is by measuring the red shift in its stretching frequency. The shift is about 200 cm^{-1} for the first reported $[\text{Ru(II)}(\text{NH}_3)_5\text{N}_2]^{2+}$ complex and increases to 400 cm^{-1} for a recently reported tris(phosphino)silyl osmium complex.[29] Gaining insights into how the chemical environment (such as the metal center and the ligand field) modulate the strength of the backward donation to N_2 will thus play an essential role in understanding the molecular mechanism of nitrogen fixation that facilitates the design of novel and highly efficient catalysts.

The strength of forwards and backwards direction of CT in the above-mentioned complexes depends on both the π-acidic ligand and the σ-acceptor moiety. To shed light on the nature of donor-acceptor interactions as well as the factors that govern their strength, one can resort to energy decomposition analysis (EDA) schemes[32–34] to unravel the effect of charge transfer (along with other binding forces) upon the formation of dative complexes. Originating from the pioneering Kitaura-Morokuma EDA,[35,36] the early variational EDA approaches define CT as the mixing of one fragment's occupied orbitals into virtuals of other fragments. Therefore, starting with molecular orbitals (MOs) optimized on each fragment, one can quantify the energy contribution associated with the CT from one fragment (A) to another (B) by evaluating the change in SCF energy upon the inclusion of the A(occupied)$\rightarrow B$(virtual) relaxations into the variational degrees of freedom. This approach was widely used in early EDA methods, such as the reduced variational space (RVS)[37] and the similar constrained space orbital variation (CSOV)[38] schemes, to identify the forward and backward CT contributions between a pair of fragments. The natural bond orbital (NBO) analysis[39,40] also employs a similar way to define CT between pairs of fragments although very different reference orbitals ("Lewis" orbitals prepared by the NBO procedure that remain strongly

orthogonal even between fragments) are employed.

The more recently developed charge transfer analysis (CTA) based on absolutely localized molecular orbitals (ALMOs)[9] is also able to separate the forward and backward CT contributions for each pair of molecules in a system. Starting from fragment orbitals that are variationally optimized within the supersystem (polarized ALMOs),[41] this approach approximates the CT stabilization energy using the energy lowering associated with a single Roothaan step, i.e., one diagonalization of the supersystem Fock matrix, which is further reformulated with unitary orbital rotations generated from a single-excitation operator ($\mathbf{X}_{vo}$).[42] The total stabilization energy can then be partitioned into contributions from forward and backward CT between different fragment pairs, which is achieved by evaluating the energetic stabilization associated with each off-diagonal block of $\mathbf{X}_{vo}$ in the polarized ALMO basis. Moreover, one can perform a singular value decomposition (SVD) on each off-diagonal block of $\mathbf{X}_{vo}$, yielding the complementary occupied-virtual pairs of orbitals (COVPs) that make the most significant contribution to the CT between a specific pair of fragments.[9]

While the schemes introduced above can separate the total CT energy into forward and backward contributions and even further into contributions from different pairs of donor and acceptor orbitals, most are unable to characterize the observable effects of CT. The recently developed adiabatic EDA scheme[43] (see Sec. 2.1) represents a systematic step forward to address this gap, which allows one to characterize the effects of CT (and other physical components) on molecular structures and vibrational frequencies. This approach has been employed to investigate observable shifts induced by intermolecular binding, such as the red or blue shifts in vibrational frequencies upon the formation of hydrogen or halogen bonds.[44–48] However, it has not been made generally possible yet to separate the observable effects of forward/backward CT in a manner that is similar to how the ALMO-CTA identifies the $A{\to}B$ and $B{\to}A$ contributions for a pair of fragments A and B,[9] even though such a partition is highly desirable in particular for interpretation purposes. One early exception was the already mentioned CSOV approach, which employed full SCF for one fragment in the

field of e.g. frozen orbitals of the other. CSOV was applied for studies of CO bound to metal atoms and clusters.[38,49,50] We note that a decomposition scheme with a similar objective was recently formulated by deriving ALMO-based linear response equations, which, nonetheless, is limited to molecular properties that are only concerned with electronic degrees of freedom, such as static polarizabilities.[51,52]

In this work, we extend the original formulation of the adiabatic ALMO-EDA by introducing two additional intermediate potential energy surfaces (PESs). Inspired by the RVS and CSOV approaches, on each of these surface one single direction of CT (either $A{\rightarrow}B$ or $B{\rightarrow}A$) is permitted while the other direction remains forbidden. The response of the acceptor fragment to such a one-directional CT, on the other hand, is captured by the intermediate state defined thereof. We obtain these "one-way" CT intermediate states via a special type of self-consistent field (SCF) calculation, whose details are given in Sec. 2.2. The variational feature of these two states renders the associated nuclear gradients readily attainable, and thus one can conveniently use them in the context of adiabatic EDA. This opens the door to an in-depth analysis for the effect of forward and backward donations on the energetic, structural, and vibrational features of dative complexes. In Sec. 4, we first validate the results produced by these two "one-way" CT states using two prototypical borane complexes (H_3N-BH_3 and $OC-BH_3$). We then utilize this approach to investigate the carbonyl complexes of beryllium oxide and carbonate (Sec. 4.2), as well as the complexes composed of a series of π-acidic ligands and the pentaammineruthenium ($[\mathrm{Ru(II)(NH_3)_5}]^{2+}$) moiety.

2 Theory

2.1 Vertical vs. Adiabatic ALMO-EDA

The ALMO-EDA scheme[17,53] separates the overall intermolecular interaction energy, ΔE_{INT}, into contributions from frozen interaction (ΔE_{FRZ}), polarization (ΔE_{POL}), and charge trans-

fer (ΔE_{CT}):

$$\Delta E_{\mathrm{INT}} = \Delta E_{\mathrm{FRZ}} + \Delta E_{\mathrm{POL}} + \Delta E_{\mathrm{CT}} \tag{1}$$

where the frozen term can be further decomposed into contributions from permanent electrostatics (ΔE_{ELEC}), Pauli repulsion ($\Delta E_{\mathrm{PAULI}}$), and dispersion interaction (ΔE_{DISP}).[53–55] Such a decomposition is usually performed at a single given geometry and thus we refer to this approach as the *vertical* ALMO-EDA thereafter. For details regarding the physical meaning and mathematical definition of each of these terms, we refer the reader to our previous publications.[53,54]

Contrasting with the vertical EDA, recently we also proposed an *adiabatic* formulation of the ALMO-EDA in order to analyze the shifts in molecular properties induced by intermolecular interactions.[43] Instead of decomposing a single-point interaction at a fixed geometry, the geometry of the complex is relaxed at the initial (isolated fragments), intermediate (frozen and polarized), and final (full complex) stages of an ALMO-EDA procedure. As in the vertical version of ALMO-EDA, the frozen state is defined as an antisymmetric product of isolated fragment wavefunctions, and the polarized state is obtained by variationally optimizing the supersystem wavefunction with respect to the orbital rotations on each fragment.[17] These electronic states correspond to distinct PESs, and the geometry relaxation on each of them is facilitated by use of the associated analytical nuclear gradients. Optimization of the isolated fragment and fully relaxed complex geometries can be achieved by employing standard SCF nuclear gradients, and the gradients for the frozen and polarized states have been previously derived by some of us.[43]

The geometry relaxation on each intermediate surface allows one to obtain information on how each intermolecular interaction component modulates the structure of a complex. Moreover, one can perform harmonic frequency calculations at the stationary points evaluated on each surface, thereby obtaining the vibrational frequency shifts induced by each physical component of the interaction.[43]

7

2.2 Generalized SCF-MI

In the original formulation of ALMO-EDA,[17] the polarized yet CT-forbidden state is obtained by using the "SCF for molecular interaction" (SCF-MI) procedure, where one variationally optimizes a fragment-block-diagonal AO-to-MO coefficient matrix with respect to the orbital rotations on each fragment. The variational space of each fragment is thus determined by the span of AO basis functions associated with the atoms that belong to the same fragment. The one-particle density matrix (1PDM) can be constructed from ALMOs using

$$\mathbf{P} = \mathbf{C}_\text{o}(\boldsymbol{\sigma}_\text{oo})^{-1}(\mathbf{C}_\text{o})^T \tag{2}$$

where $\mathbf{C}_\text{o}$ refers to the MO coefficients for the occupied ALMOs, and $\boldsymbol{\sigma}_\text{oo}$ denotes their overlap metric, which is obtained by transforming the AO overlap matrix ($\mathbf{S}$) into the basis formed by these occupied ALMOs:

$$\boldsymbol{\sigma}_\text{oo} = (\mathbf{C}_\text{o})^T \mathbf{S} \mathbf{C}_\text{o} \tag{3}$$

The energy functional, $E = E[\mathbf{P}]$, can be minimized by solving locally projected SCF equations[41,56,57] or using gradient-based optimization algorithms (with respect to on-fragment orbital rotations).[58]

By introducing the concept of *fragment variational subspaces*, we propose a generalized formulation of SCF-MI. For a given fragment A, instead of using its full AO span ($\mathbb{I}_A$), we define its variational degrees of freedom as $\mathbb{G}_A$, where $\mathbb{G}_A$ is the space spanned by a set of vectors whose expansion coefficients in the AO basis are given by a matrix $\mathbf{G}_A$, i.e., $\mathbb{G}_A = \text{span}\{\mathbf{G}_A\}$. The concatenation of subspace vectors for each fragment, $\mathbf{G} = [\mathbf{G}_A, \mathbf{G}_B, ...]$, defines the effective working basis for SCF-MI. The MOs can thus be represented as linear combinations of vectors in $\mathbf{G}$, whose coefficients are denoted as $\mathbf{C}^G = [\mathbf{C}_\text{o}^G, \mathbf{C}_\text{v}^G]$. By left-

multiplying $\mathbf{C}^G$ with $\mathbf{G}$, one can retrieve the AO-to-MO coefficient matrix:

$$\mathbf{C} = [\mathbf{C}_{\mathrm{o}}, \mathbf{C}_{\mathrm{v}}] = \mathbf{G}[\mathbf{C}_{\mathrm{o}}^G, \mathbf{C}_{\mathrm{v}}^G] \tag{4}$$

and the 1PDM can thus still be calculated via Eq. (2).

Within generalized SCF-MI, one only requires $\mathbf{C}^G$ to be fragment-block-diagonal, while the vectors that span the variational subspace of a given fragment ($\mathbf{G}_A$, $\mathbf{G}_B$, ...) are allowed to be expanded by AO basis functions centered on other fragments. The vectors in $\mathbf{G}$ that belong to the same fragment are orthonormalized against each other for convenience, while interfragment orthogonality is usually not enforced. It is evident that the generalized SCF-MI scheme imposes a weaker constraint on the MO coefficient matrix than the original ALMO definition since the AO-to-MO coefficient matrix $\mathbf{C}$ need no longer be "absolutely localized", and in fact, if one chooses $\mathbb{G}_A = \mathbb{I}_A$ for each fragment, the original AO-based ALMO results will be recovered by generalized SCF-MI. Nevertheless, as $\mathbf{C}^G$ has a fragment-block-diagonal structure just like the $\mathbf{C}$ matrix in the original scheme, similar equations still hold for generalized SCF-MI once the quantities are properly transformed into the basis defined by $\mathbf{G}$. In Sec. S1 in the Supporting Information (SI), we show the the locally projected SCF equation and the energy gradient with respect to on-fragment orbital rotations for generalized SCF-MI.

The generalized SCF-MI scheme was originally proposed to allow for a truncated virtual space for each fragment being used in the polarization step of ALMO-EDA,[58] thus providing a well-defined separation between polarization and charge transfer. In addition to that, by modifying the content of $\mathbf{G}$, one can solve a broad spectrum of variational optimization problems with varying degrees of freedom using the SCF-MI procedure. As an extreme example, if one uses the full AO span of the whole system ($\mathbb{I}$) as the variational subspace for each fragment, the full SCF result will be recovered by performing a generalized SCF-MI calculation.

2.3 Variational Forward-Backward Analysis of the CT contribution

Making use of the flexibility in variational space offered by generalized SCF-MI, we introduce two additional intermediate states into the ALMO-EDA. For a system comprising two fragments, we first denote the converged orbitals (expanded in AOs) at the polarization step as $[\mathbf{C}_{o,A}, \mathbf{C}_{v,A}] \cup [\mathbf{C}_{o,B}, \mathbf{C}_{v,B}]$, which are absolutely localized on fragments A and B, respectively. Note that within generalized SCF-MI, these orbitals can be used to define the variational space for the polarized wavefunction (shown as stage (a) in Fig. 1), and the corresponding MO coefficient matrix $\mathbf{C}^G$, according to Eq. (4), will be an identity matrix ($\mathbf{I}$). We then construct the virtual space for the full system that is strongly orthogonal to the occupied space, which is spanned by the orthonormalized projected virtual orbitals. The projected virtuals are defined as

$$\mathbf{C}_{v,\text{proj}} = (\mathbf{I} - \mathbf{PS})\mathbf{C}_v \tag{5}$$

and the orthonormalized vectors, $\mathbf{C}_{v,\text{full}}$, are obtained through a canonical orthogonalization[59] of $\mathbf{C}_{v,\text{proj}}$.

Now we construct two "one-way" CT surfaces: on the first surface, we allow $\mathbf{C}_{o,A}$ to be mixed with $\mathbf{C}_{v,\text{full}}$ and $\mathbf{C}_{o,B}$ with $\mathbf{C}_{v,B}$, thus the corresponding $\mathbf{G}$ matrix has the form $[\mathbf{C}_{o,A}, \mathbf{C}_{v,\text{full}}] \cup [\mathbf{C}_{o,B}, \mathbf{C}_{v,B}]$ (stage (b) in Fig. 1); on the second surface, we allow $\mathbf{C}_{o,B}$ to be mixed with $\mathbf{C}_{v,\text{full}}$ while $\mathbf{C}_{o,A}$ only with $\mathbf{C}_{v,A}$, and the corresponding $\mathbf{G}$ matrix is $[\mathbf{C}_{o,A}, \mathbf{C}_{v,A}] \cup [\mathbf{C}_{o,B}, \mathbf{C}_{v,\text{full}}]$ (stage (c) in Fig. 1). From the choice of variational spaces one can infer that $A{\to}B$ donation (but not $B{\to}A$) is allowed on the first of of these two surfaces, and that the response of the acceptor fragment B, also known as "repolarization", is also captured. The second surface is the reverse: $B{\to}A$ donation (but not $A{\to}B$) is allowed, with A being repolarized. Finally, as we mentioned above, if one chooses $\mathbf{G}$ to be $[\mathbf{C}_{o,A}, \mathbf{C}_{v,\text{full}}] \cup [\mathbf{C}_{o,B}, \mathbf{C}_{v,\text{full}}]$ (stage (d) in Fig. 1), the fully relaxed SCF surface will be recovered.

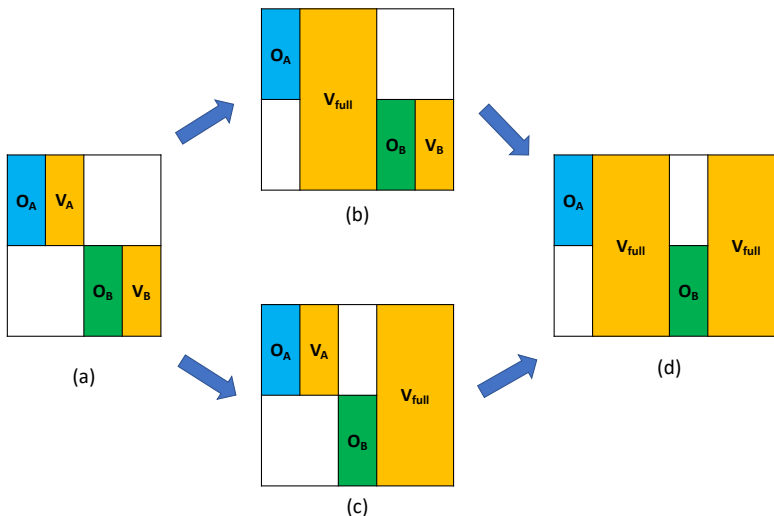We note that the construction of these two "one-way" CT states is inspired by the previ-

Figure 1: The form of **G** matrix in generalized SCF-MI at four different stages in adiabatic ALMO-EDA: (a) the polarized state without CT; (b) the $A{\rightarrow}B$ one-way CT state; (c) the $B{\rightarrow}A$ one-way CT state; (d) the fully relaxed SCF state.

ously developed RVS[37] and CSOV[38] schemes. One notable difference is that in these previous methods the variational space is constructed from orbitals calculated at the isolated fragment level, while here we start from variationally optimized ALMOs obtained in the polarization step. In addition, in RVS and CSOV only the occupied orbitals on the donor fragment are relaxed while the acceptor fragment orbitals are frozen in their initial shape when considering a given direction of CT; in contrast, in our scheme both fragments are variationally relaxed on these "one-way" CT surfaces. For brevity, in the following we refer to our approach as illustrated in Fig. 1 as the *variational forward-backward* (VFB) analysis.

The overall CT stabilization energy in ALMO-EDA is defined as

$$\Delta E_{\text{CT}} = E_{\text{Tot}} - E_{\text{Pol}} \tag{6}$$

where E_{Tot} is the unconstrained, fully relaxed SCF energy of the supersystem and E_{Pol} the energy of the polarized yet CT-forbidden state that is represented by Fig. 1(a). The stabilization effect of each direction of CT, denoted as ΔE_{CTf} $(A{\rightarrow}B)$ and ΔE_{CTb} $(B{\rightarrow}A)$,

can be analogously defined:

$$\Delta E_{\text{CTf}} = E_{\text{CTf}} - E_{\text{Pol}} \qquad (7)$$

$$\Delta E_{\text{CTb}} = E_{\text{CTb}} - E_{\text{Pol}} \qquad (8)$$

where E_{CTf} and E_{CTb} are the energies of the variational forward and backward states represented by Figs.1(b) and 1(c), respectively. We adopt this convention because in our later examples we consistently choose fragment A to be a typical σ-donating Lewis base, such as NH_3, CO, etc., and fragment B a Lewis acidic moiety (e.g. BH_3 or $[\text{Ru}(NH_3)_5]^{2+}$). The total charge transfer energy can thus be partitioned into three terms:

$$\Delta E_{\text{CT}} = \Delta E_{\text{CTf}} + \Delta E_{\text{CTb}} + \Delta E_{\text{HO}} \qquad (9)$$

where the higher-order (HO) term captures the non-additive contribution to energetic stabilization arising from the relaxation of electronic structure when both directions of CT are permitted simultaneously. This term is negative and relatively small in all examples investigated in this work (1–3% of the overall strength of ΔE_{CT} for the main group complexes and around 10% for the transition metal complexes). One should note that in the original ALMO-CTA scheme[9] the decomposition of the CT energy also yields the three terms on the right-hand side of Eq. (9) but uses a single *non-iterative* Roothaan-step correction upon the converged ALMO polarized state. Therefore, our scheme based on generalized SCF-MI serves as an alternative approach to decompose the energetic stabilization of CT with the advantage that the energies of the forward and backward CT states are strict upper bound to the full SCF energy. The results of these two approaches will be compared in Sec. 4.

One desirable feature of the present VFB scheme is that the forces associated with these two "one-way" CT states can be evaluated in the same way as the nuclear gradients for the polarized (AO-based SCF-MI) and fully relaxed (standard SCF) states (see SI Sec. S2 for the mathematical details). Therefore, one can readily augment the adiabatic ALMO-EDA

scheme with the PESs of these additional VFB states.

3 Computational Details

The generalized SCF-MI scheme has been implemented in the released version of Q-Chem 5.0.[60] On top of that, we enabled the energy and force calculations for the VFB "one-way" CT states in a locally developed version so that they can be integrated into the adiabatic ALMO-EDA framework. The original AO-based SCF-MI scheme[41] is utilized in both vertical and adiabatic EDA calculations to separate the polarization and charge transfer contributions. To validate the CT energy decomposition results given by our VFB scheme, we compared them against the results of the original perturbative ALMO-CTA.[9] The latter approach was also used to generate the COVPs that help identify the key donor and acceptor orbitals. The COVP orbitals are plotted with an isovalue of 0.1 a.u. and density difference plots with an isovalue of 0.01 a.u.

All the energy and molecular property calculations were performed using the B3LYP functional[61–63] in combination with the def2-TZVPP[64] basis set unless otherwise specified. For the $4d$ transition metals (Ru and Tc), an effective core potential[65] was employed. The B3LYP functional was chosen because it provides adequate accuracy for CT-dominated complexes[66] and also decent agreement with experimental vibrational frequency shifts in all three application examples discussed in this work. In addition, we repeated all the calculations with two other functionals (B97-D[67] and ωB97X-D[68]). The functionals tested range from pure GGA (B97-D) to global and range-separated hybrid GGAs (B3LYP and ωB97X-D, respectively) and thus exhibit different extents of charge delocalization errors,[69] which consequently lead to the discrepancies in the predicted strength of CT and in the magnitude of frequency shift obtained. In general, B97-D produces the most red-shifted frequencies and ωB97X-D the least, since delocalization errors are largest for the pure GGA, and smallest for the range-separated hybrid. Nonetheless, our results demonstrate that the qualitative

trends given by the VFB analysis can all be reproduced with either of the three functionals (see Tables S2, S5–S7, and S9–S13 in the SI).

The optimized structures on different PESs were verified as true minima by examining the lowest harmonic frequency, and all the vibrational frequencies were computed with a finite-difference approach using the analytical nuclear gradients associated with each PES, for which the step size of atomic position displacement was set to be 10^{-3} Å. In Sec. 4, we report the frequency shift in the stretching mode of diatomic ligands N_2, CO, and BF (denoted by XY) relative to that calculated in the *isolated* (uncoordinated) state:

$$\Delta\nu_{XY} = \nu_{XY}(\text{complex}) - \nu_{XY}(\text{free}) \tag{10}$$

A negative value of $\Delta\nu_{XY}$ corresponds to frequency red shift and a positive value blue shift. The adiabatic EDA framework allows one to locate the energy minimum and obtain the associated harmonic frequencies on each individual PES: frozen (Frz), polarized (Pol), forward CT (CTf), backward CT (CTb) and fully relaxed (Tot).

As the geometry of a complex relaxes when moving from one PES to another, the shift in vibrational frequency calculated in such an adiabatic fashion arises not only from the distinction in constraints applied to different electronic states (i.e. the four states illustrated in Fig. 1) but also from the change in molecular structure. For instance, the inclusion of CT usually shortens the intermolecular distance, which, however, also enhances other effects such as those from electrostatic interactions. In order to estimate the strength of both the electronic and geometric effects of CT, one can perform a constrained geometry optimization in the Pol state with the intermolecular distance fixed at the CTf/CTb minimum-energy distance followed by a frequency calculation. The frequencies obtained thereof are denoted as $\nu_{XY}(\text{Pol@CTf})$ and $\nu_{XY}(\text{Pol@CTb})$, whose respective differences from the adiabatic CTf and CTb frequencies correspond to the pure electronic effect of forward and backward donation

14

on the vibrational frequency shift:

$$\Delta\nu^{\text{eff}}(\text{CTx}) = \nu_{\text{XY}}(\text{CTx}) - \nu_{\text{XY}}(\text{Pol@CTx}) \tag{11}$$

where CTx stands for either CTf or CTb.

4 Results

4.1 Borane Complexes

The VFB decomposition of CT (see Sec. 2.3) yields two new PESs on which only one direction of CT is permitted. As the first step to validate this method, we analyze the H_3N-BH_3 complex in which the $H_3N{\rightarrow}BH_3$ forward donation dominates (see the large forward vs. backward ratio for this complex in Table 1). As shown in the left panel of Fig. 2, the surface that allows forward donation only (denoted as CTf) stays fairly close to the fully relaxed PES (Tot), whereas the one with $H_3N{\leftarrow}BH_3$ backward donation only (denoted as CTb) close to the Pol surface, confirming that these two newly introduced intermediate states describe this simple mono-directional CT correctly.
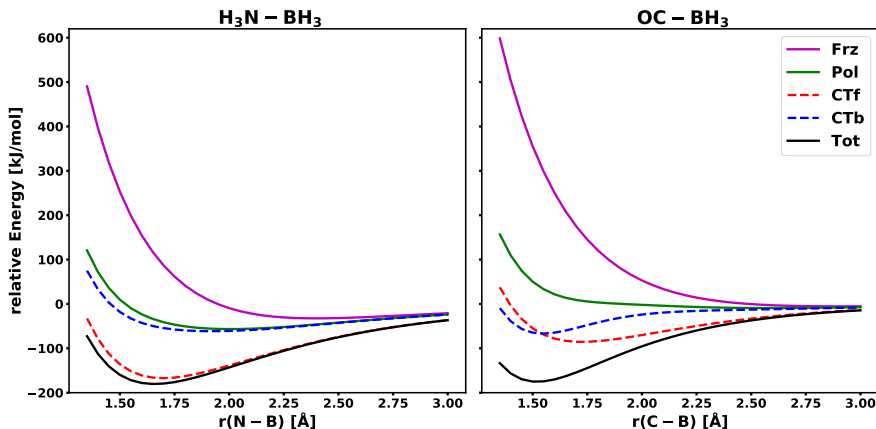

Figure 2: Potential energy surface (rigid scan) for each ALMO-EDA intermediate state (Frz, Pol, CTf, CTb, and Tot) for the two borane complexes. Left panel: H_3N-BH_3; right panel: $OC-BH_3$.

We then move to the OC−BH$_3$ adduct that is known to have more involved bi-directional CT as many other carbonyl compounds do: a σ-type forward donation (OC→BH$_3$) from the lone pair on CO into the empty p orbital on boron, and a π-type backbonding (OC←BH$_3$) from the B−H σ bonding orbitals to CO's empty π^* level, which are illustrated by the COVPs shown in Fig. 3. The vertical EDA results for this complex, as given in Table 1, reveal its strongly repulsive frozen interaction as well as the substantially favorable polarization and CT contributions. A further decomposition of the CT energy using the scheme introduced in this work suggests that the two directions of CT contribute almost equally in this complex.

Table 1: Vertical ALMO-EDA results for H$_3$N−BH$_3$ and OC−BH$_3$. The energies are in kJ/mol and the distance in Å. The ratio refers to $\Delta E_{CTf}/\Delta E_{CTb}$.

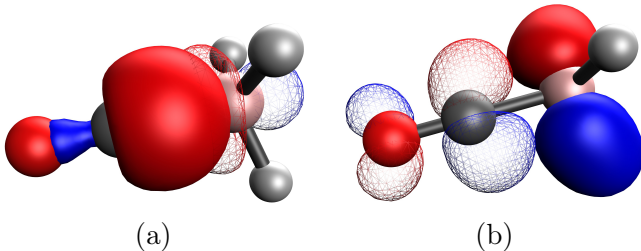| molecule	ΔE_{Frz}	ΔE_{Pol}	ΔE_{CTf}	ΔE_{CTb}	ΔE_{CT}	ΔE_{Tot}	ratio	r(X−B)
H$_3$N−BH$_3$	112.3	−147.2	−131.4	−15.6	−145.4	−180.3	8.0	1.658
OC−BH$_3$	331.8	−289.0	−104.0	−108.9	−218.1	−175.3	1.0	1.520

(a)   (b)

Figure 3: The key COVPs in OC−BH$_3$ that illustrate its bi-directional CT: (a) σ-type and (b) π-type. The donor orbtial is shown as a solid isosurface while the acceptor orbital is shown as a mesh isosurface).

The five intermediate surfaces (Frz, Pol, CTf, CTb, and Tot) for OC−BH$_3$ are shown in the right panel of Fig. 2. While the vertical EDA results (Table 1) suggest that the forward and backward CT are almost equally strong for this system, one should note that this actually only holds around the equilibrium N−B distance. Another remarkable feature is that the π-type backbonding decays faster than the forward donation right beyond the equilibrium, rendering the latter as the dominant contribution to CT at long range. As shown in SI Fig. S1, this behavior can also be reproduced with the forward and backward

16

CT contributions obtained from the perturbative ALMO-CTA.[9] This finding also holds for the metal complexes (see Figs. 5 and 10) and might be useful for kinetic control of carbonyl insertion/elimination reactions as the M−CO distance is usually elongated in transition states, where the forward CT plays a dominant role in the donor-acceptor interaction. In addition, Fig. S1 also demonstrates that the forward and backward CT are dominated by the σ-type and the π-type COVPs, respectively, as the two perturbative stabilization energies are almost fully recovered by their dominant COVPs.

Table 2: Adiabatic ALMO-EDA results for the structural and vibrational parameters of OC−BH$_3$ complex. $\Delta r(CO)$ and $\Delta \nu_{CO}$ refer to changes relative to the values of a free CO molecule (r(CO) = 1.125 Å and ν_{CO} = 2216 cm^{-1}). The experimental values are taken from Refs. 70 and 71.

Surface	r(CB) [Å]	$\Delta r(CO)$ [Å]	$\Delta \nu_{CO}$ [cm^{-1}]
Frz	3.29	−0.001	8
Pol	3.18	−0.001	9
CTf	1.77	−0.010	108
CTb	1.54	0.001	24
Tot	1.52	0.004	−2
Exp	1.54	0.003	22

The importance of CT for this interaction is further highlighted by the adiabatic ALMO-EDA results (Table 2). On the fully relaxed surface, the obtained C−B and C−O bond distances and the shifts in ν_{CO} are in reasonable agreement with the previous theoretical studies and experimental values.[16,70–72] The non-CT binding forces (frozen interaction and polarization) yield only a weakly bound adduct with the C−B distance, r(CB), being over 3 Å, and r(CB) is only shortened by ∼0.2 Å upon moving from the Frz to Pol surface. Allowing only forward donation drastically reduces the C−B distance to 1.77 Å, and with backward CT only the C−B distance is shortened even more, yielding a C−B distance of 1.54 Å that is already very close to the full equilibrium distance. The extraordinarily shortened inter-molecular distance obtained on the CTb surface can be rationalized by the relatively weak Pauli repulsion in this complex, which is almost fully compensated by the favorable perma-

nent electrostatics and polarization contributions even at a short intermolecular distance, and also by the rapid decay of CTb beyond equilibrium. This is in contrast to the transition metal complex cases (*vide infra*) where the synergy of CTf and CTb is required to overcome the stronger Pauli repulsion.

The calculated ν_{CO} on the fully relaxed surface is marginally red-shifted, while that on the Pol surface exhibits a small blue shift. The latter is in line with our previous work[45,73] as well as other studies showing blue shifts in CO stretching frequency in the presence of an electric field along the C→O direction, such as in complexes where CO is bound to a metal cation,[74,75] which is known as molecular Stark effect. This is because the dipole moment of CO increases when the C−O bond is contracted, which is favored by the electrostatic interaction between CO and the positively charged moiety. The blue shift is most prominent on the PES with forward CT only (CTf), which can be attributed to two effects: (i) the forward donation itself (electronic) and (ii) the shortened intermolecular distance r(CB) (geometric) that enhances the electrostatic interaction. The significance of these two effects can be estimated by optimizing the geometry of this complex in the Pol state with the C−B distance *constrained* at the minimum-energy r(CB) on the CTf surface (1.77 Å) and then evaluating the frequency shift. A blue shift of 105 cm^{-1} is obtained in this "Pol@CTf" state, which is almost identical to the blue shift on the CTf surface (108 cm^{-1}), indicating that the large blue shift caused by forward CT is almost solely a geometric effect, i.e., enhanced electrostatic interaction due to the shortened C−B distance.

With backward CT only, ν_{CO} is also moderately blue-shifted (24 cm^{-1}), for which the geometric and electronic effects can be separated in the same way as described above. With r(CB) fixed at 1.54 Å, the "Pol@CTb" frequency is significantly more blue-shifted ($+184$ cm^{-1} relative to free CO) than the "CTb@CTb" frequency, indicating that the back-donation, as expected, results in an effective red shift of 160 cm^{-1} by modifying the electronic structure of the CO moiety. This result, as well as the very small $\Delta\nu_{CO}$ in the fully relaxed complex, suggests that the shift in ν_{CO} is not always a reliable indicator for the strength of back-

donation, as it can be largely compensated by the competing electrostatic force that blue-shifts ν_{CO}, which is nicely illustrated by this example. These results are in line with previous discussions in literature,[9,72,74] while our VFB approach is able to directly identify the origin of shifts in r(CB), Δr(CO), and $\Delta\nu_{CO}$.

In summary, our analysis of the two borane adducts above demonstrates that the VFB decomposition of charge-transfer effects yields qualitatively correct results as one would expect for these systems, validating its use in the applications presented below. It not only serves as an alternative scheme to separate the entire CT stabilization energy into forward and backward contributions, but also directly probes their effects on shifts in observables.

4.2 Binding of CO with BeO and $BeCO_3$

A combined spectroscopic and theoretical study by Frenking *et al.*[76] investigated the binding of CO with beryllium oxide and carbonate (BeY with Y = O or CO_3) as well as the shifts in CO's stretching frequency (ν_{CO}). These beryllium compounds are strong Lewis acids that are even able to form adducts with noble gases.[77] In their study, carbonyl adducts of two binding modes with either the carbon or oxygen atom of CO interacting with the BeY moiety were isolated and characterized by IR spectroscopy,[76] which are denoted as the κC and κO modes in the following discussion, respectively. It was shown that ν_{CO} is red-shifted for κO carbonyls (-80 cm^{-1} for CO$-$BeO and -53 cm^{-1} for CO$-$BeCO$_3$) while blue-shifted for the κC isomers (43 cm^{-1} for OC$-$BeO and 122 cm^{-1} for OC$-$BeCO$_3$). The theoretical investigation demonstrated that the magnitude of interaction energies follows the order OC$-$BeO > OC$-$BeCO$_3$ > CO$-$BeO > CO$-$BeCO$_3$. Interestingly, the more strongly bound OC$-$BeO exhibits a significantly smaller blue shift than OC$-$BeCO$_3$. The EDA-NOCV (natural orbital for chemical valence)[34,78] analysis for the two κC complexes revealed that their σ-type forward donations (OC$\rightarrow$BeY) are of similar strengths, while the π-type back-donation (OC$\leftarrow$BeY) is more pronounced in OC$-$BeO, which explained both its stronger interaction energy and less blue-shifted ν_{CO}. For the κO complexes, the

Table 3: Vertical ALMO-EDA results (energies in kJ/mol) for the four BeY–carbonyl adducts. The ratio corresponds to the value of E_{CTf}/E_{CTb} for each complex.

Adduct	ΔE_{Frz}	ΔE_{Pol}	ΔE_{CTf}	ΔE_{CTb}	ΔE_{CT}	ΔE_{Tot}	ratio
OC−BeO	11.4	−108.8	−26.5	−49.2	−77.9	−175.2	0.5
CO−BeO	31.4	−78.4	−29.8	−24.2	−54.9	−101.9	1.2
OC−BeCO$_3$	12.7	−93.9	−29.5	−14.9	−44.9	−126.1	2.0
CO−BeCO$_3$	27.0	−69.0	−28.3	−7.2	−35.6	−77.7	4.0

contribution from CT is slightly weaker and the σ and π donations are of similar strength. Therefore, instead of backward CT, the authors attributed the red-shifted ν_{CO} in the κO complexes to the "reversed polarization" of CO relative to the κC complexes, which makes the C−O bond longer and less polar.

We compare the previous findings with the results of our more detailed VFB-EDA analysis including a decomposition of the shifts in ν_{CO}. The ALMO-EDA results at the equilibrium geometries of these four complexes (Table 3) are analyzed first. The comparison between the κC and κO binding modes for BeO reveals that the former is more stable by over 70 kJ/mol, and the difference is evenly distributed over all three EDA terms. The difference in ΔE_{Frz} results from the substantially more favorable electrostatic interaction under the κC mode, which overcomes its stronger Pauli repulsion. Upon polarization, one can observe a reduction of electron density on the distant atom for both binding modes, which is shown in Fig. S2. The difference between their CT energies is mainly caused by the stronger back-donation in the κC complex (see Table 3), which can be rationalized via the COVPs obtained from the perturbative CT analysis (Fig. 4(a) and SI Figs. S4(c)–(e)): under the κC mode, the π^* acceptor orbital of CO (Fig. S4(d)) has a better overlap with the π-donor orbital of BeO (Fig. S4(c)) than that under the κO mode (Fig. S4(e)), since the π^* orbital of CO is polarized towards the C atom.

The comparison between the BeO and BeCO$_3$ complexes (see Table 3) indicates that the carbonate analogues bind CO less strongly than the oxides mainly because of their less favorable CT contributions. The CTf/CTb ratios for the BeCO$_3$ complexes reveal the
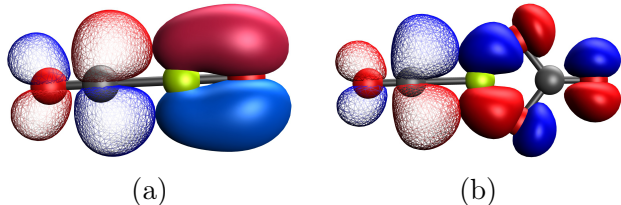
Figure 4: Key COVPs contrasting the π backbonding for both OC$-$BeY complexes: (a) OC$-$BeO: (b) OC$-$BeCO$_3$. The donor orbitals are in solid colors and the acceptor orbitals are meshed.
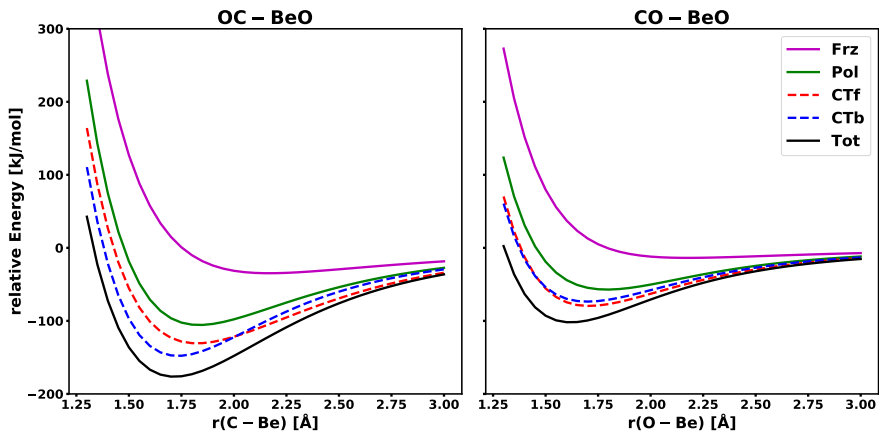

Figure 5: Potential energy surface (rigid scan) for each ALMO-EDA intermediate state (Frz, Pol, CTf, CTb, and Tot) for OC$-$BeO (left) and CO$-$BeO (right).

weaker back-donation in these complexes, which is consistent with the previous EDA-NOCV results.[76] This can be elucidated by the smaller overlap between the π-donor orbital on BeCO$_3$ with the π^* orbital on CO as illustrated in Fig. 4. The comparison between the κC and κO isomers of the carbonate complex, on the other hand, shows the same trend as for the above-discussed BeO complexes. Finally, we note that the higher-order contribution is very small for this set of systems (3% of the overall CT energy for the complexes with BeO and $\sim$1% for those with BeCO$_3$), indicating that the decomposition of CT stabilization energy using the VFB approach yields nearly additive results for these Be complexes.

The PES scans for OC$-$BeO and CO$-$BeO are shown in Fig. 5. Both isomers (κC and κO) are only weakly bound in the frozen state with shallow minima located at 2.15 and 2.17 Å, respectively. Polarization strengthens the interactions and shortens the equilibrium Be$-$X distances of both isomers significantly. The κC complex is of a larger polarization

energy, which can be rationalized by the chemically softer lone pair located on the C atom. Interestingly, given the characteristic difference between the lone pairs located on C and O, the energetic contributions from forward donation (from CO/OC to BeO) are of similar magnitude for these two complexes in the range of 1.5–1.8 Å. Nevertheless, the energetic contribution of forward CT (energy lowering relative to the Pol surface) does show a slower decay to zero in the long range under the κC mode, as one would expect based on the more diffuse electron lone pair on the C atom (see Fig. S5 in the SI). The backward donation, on the other hand, is of a greater strength in the κC complex, which is in line with the vertical EDA results that were discussed above (Table 3). The strong back-donation in the κC complex also leads to a reduction of the Be−C distance by 0.1 Å, and the resulting intermolecular distance is only 0.016 Å longer than the full equilibrium distance.

The most pronounced difference between these two binding modes is observed when comparing their CTf against CTb surfaces for each of them: for CO−BeO, the forward and backward donations yield very similar energetic stabilization relative to the Pol state at all ranges; by contrast, OC−BeO exhibits markedly stronger backward CT than forward around the minimum-energy distance while the back-donation decays more rapidly, resulting in a crossover around 2 Å. Note that the faster decay of backward CT was also observed in the OC−BH$_3$ example discussed above (Sec. 4.1). Altogether, the CO molecule binds with BeO more strongly under the κC mode mainly because of the more favorable polarization and backward CT contributions. It is noteworthy that the equilibrium Be−X distance on the fully relaxed surface appears to be longer for the κC complex despite its stronger interaction. This, once again, can be rationalized by the more diffuse lone pair (σ-donor orbital) as well as the larger amplitude of the π-acceptor orbital on the C atom, with the former rendering the κC complex more prone to Pauli repulsion and thus energetically less favorable at a short distance, and the latter facilitating a considerable interaction strength at a comparatively large intermolecular separation.

The adiabatic ALMO-EDA results for OC−BeO and CO−BeO are shown in Table 4.

The carbonyl stretching frequency (ν_{CO}) is blue-shifted by 102 cm^{-1} for the κC complex at the Frz level, accompanied by a contraction of the C$-$O bond by 0.01 Å. In contrast, the κO complex exhibits a moderate red shift of -28 cm^{-1} relative to the free ν_{CO} and correspondingly a lengthened C$-$O bond (by 0.004 Å). While Ref. 76 assigned the origin of the opposite frequency shifts in OC$-$BeO and CO$-$BeO to the "reversed polarization" of the C$-$O bond in these two complexes, our adiabatic ALMO-EDA results reveal that the respective blue and red shifts in these two complexes already appear on the frozen surface where *no* orbital interaction (polarization or charge transfer) is involved. According to this result, one can elucidate the opposite shifts in ν_{CO} for these two complexes through the molecular Stark effect: since the Be atom carries partial positive charge and the dipole moment of CO (with oxygen as the positive end) increases upon the contraction of the C$-$O bond, a shortened C$-$O bond enhances the attractive electrostatic interaction and therefore is energetically favored, rendering ν_{CO} blue-shifted; on the contrary, a lengthened C$-$O bond is more favored by the electrostatic interaction in CO$-$BeO due to the opposite orientation of CO's permanent dipole, resulting in a red shift in ν_{CO}. These results are in agreement with the previous studies on classical (neutral) and non-classical (cationic) metal carbonyls.[45,73–75,79,80]

The inclusion of polarization further enhances both the blue shift in CO$-$BeO and the red shift in OC$-$BeO. However, as the frequency shifts on the Pol surface are calculated at shortened intermolecular distances relative to those on Frz, these more pronounced frequency shifts again arise from both the geometric and electronic effects. While the forward donation to BeY imposes insignificant effects on the bond length and stretching frequency of CO, the back-donation substantially lowers ν_{CO} under both the κC and κO modes. With bi-directional CT, their ν_{CO}'s are further red-shifted relative to those on the CTb surface, which can be attributed to the non-additive relaxation of their electronic structure.

The two BeCO$_3$ complexes exhibit shifts in ν_{CO} that are comparable to those of the corresponding BeO complexes on the Frz, Pol, and CTf surfaces. The most pronounced

Table 4: Adiabatic ALMO-EDA results for the four X−BeY adducts (for a free CO molecule r(CO) = 1.125 Å and ν_{CO} = 2216 cm^{-1}). The distances are in Å and frequencies in cm^{-1}.

Property	Surface	OC−BeO	CO−BeO	OC−BeCO$_3$	CO−BeCO$_3$
r(CO)	Frz	1.115	1.129	1.117	1.129
r(CO)	Pol	1.112	1.132	1.113	1.132
r(CO)	CTf	1.112	1.133	1.112	1.134
r(CO)	CTb	1.121	1.137	1.114	1.132
r(CO)	Tot	1.122	1.141	1.115	1.135
r(X-Be)	Frz	2.148	2.167	2.345	2.324
r(X-Be)	Pol	1.833	1.793	1.888	1.845
r(X-Be)	CTf	1.823	1.707	1.868	1.727
r(X-Be)	CTb	1.733	1.700	1.831	1.812
r(X-Be)	Tot	1.717	1.620	1.810	1.695
$\Delta\nu_{CO}$	Frz	102	−28	80	−28
$\Delta\nu_{CO}$	Pol	141	−42	130	−46
$\Delta\nu_{CO}$	CTf	140	−51	133	−59
$\Delta\nu_{CO}$	CTb	44	−115	101	−54
$\Delta\nu_{CO}$	Tot	31	−160	95	−76
$\Delta\nu_{CO}$	Exp	43	−80	122	−53

difference originates from the much weaker backbonding from BeCO$_3$ than that from BeO, which is reflected in the much smaller changes in ν_{CO} from Pol to CTb for the BeCO$_3$ complexes (see Table 4). This is also consistent with the vertical EDA results shown in Table 3. Therefore, the significant blue shift in the fully relaxed OC−BeCO$_3$ complex is a consequence of the strong Stark effect, which significantly shortens the C−O bond and increases its stretching frequency, complemented with the weak back-donation from BeCO$_3$ that is inadequate to compensate for the blue-shifting effect.

The discussion in Sec. 4.1 regarding the shift in ν_{CO} nicely revealed that the enhanced electrostatic interaction upon the shortening of r(C−B) is the main contributor to the frequency shift on the CTf surface by calculating ν_{CO} in the "Pol@CTf" state. Here we employ a similar analysis to investigate the distance dependence of the effects of Frz, Pol, CTf, and CTb on ν_{CO}. Specific attention is paid to the shifts induced by each energy component at the full equilibrium X−Be distances (e.g. Frz@Tot) since all these effects are at their maximum

strength there. For both OC−BeO and CO−BeO, we performed constrained geometry opti-
mizations on each intermediate surface with r(X−Be) fixed at varying values and evaluated
ν_{CO} at each given distance. The resulting frequency shifts relative to the free CO stretching
frequency, which are denoted as $\Delta\nu_{CO}$, are plotted in Fig. 6 as a function of r(X−Be). It is
clearly revealed that the overall frequency shifts are mainly determined by how the strength
of permanent electrostatics, which is encompassed in the frozen term, compares to that of
backward CT, and that both polarization and forward CT only result in moderate red shifts
relative to ν_{CO} on the Frz surface. At the minimum-energy distance on the Tot surface, the
CO−BeO isomer exhibits a minimal blue shift on the frozen surface ($+13$ cm^{-1} relative to
free CO), small but still sizable red shifts induced by Pol (-44 cm^{-1} relative to Frz) and CTf
(-13 cm^{-1} relative to Pol), and a significant red shift caused by CTb (-85 cm^{-1} relative to
Pol). In contrast, the OC−BeO isomer exhibits a much more considerable blue shift on the
frozen surface ($+199$ cm^{-1} relative to free CO). Despite the substantial red shift associated
with the backward CT (-127 cm^{-1} relative to Pol), it is still inadequate to compensate for
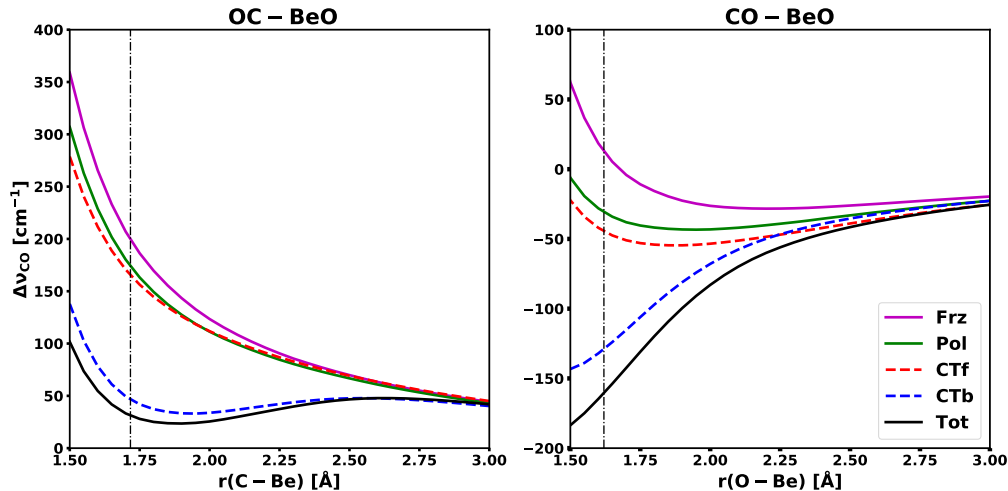the strong blue shift induced by frozen interaction, leading to an overall blue-shifted ν_{CO}.

Figure 6: Shift in ν_{CO} (in cm^{-1}) as a function of the intermolecular distance in each interme-
diate state (relative to free CO) for OC−BeO (left) and CO−BeO (right). The frequencies
are evaluated at complex geometries relaxed at each given Be−X distance. The black dashed
lines indicate the full equilibrium distance for each complex.

In summary, our VFB-EDA analysis reveals that the distinct frequency shifts in the κC

and κO complexes of beryllium oxide and carbonate result from the competition between the electrostatic interaction and the backward CT from BeO or BeCO$_3$ to CO. The electrostatic interaction affects the CO stretching frequency through the Stark effect, rendering ν_{CO} strongly blue-shifted for the κC motif while moderately red-shifted for κO. Polarization and forward CT further increase the blue or red shift, mainly by shortening the intermolecular distance, which leads to enhanced Stark effect. The backward CT, which is more pronounced in the complexes with BeO, weakens the C$-$O bond under both binding modes. It offsets the blue shifts in the κC complexes while further red-shifts ν_{CO} in the κO ones. The results for the κO complexes demonstrate that significant red shift in ν_{CO} is possible even with a weak back-donation if it is aligned with the electrostatic effect. Our results agree with Ref. 76 in explaining the stronger blue shift in OC$-$BeCO$_3$ than in OC$-$BeO while providing a distinct explanation for the opposite frequency shifts in the κC and κO complexes.

4.3 Pentaammineruthenium(II) Complexes of the Isoelectronic N$_2$, CO and BF

The red shift in CO or N$_2$'s stretching frequency is often used as an indicator for the strength of the π-type metal-to-ligand back-donation, whereas the effect of the forward donation on this vibrational mode is small due to the non-bonding character of the σ-donating orbital (lone pair on the ligand).[74,75,81] Bistoni *et al.* recently investigated the effects of both σ forward and π backward donations on the C$-$O bond length and its stretching frequency using charge displacement analysis[82,83] with a large set of classical and non-classical carbonyl complexes.[80] They found that ν_{CO} and r(CO) are in very good correlation with the strength of the π back-donation but not with the strength of the σ forward donation. The blue shift in non-classical carbonyl complexes, on the other hand, stems mainly from electrostatic interaction and polarization due to the positively charged metal moiety. Using the block-localized wavefunction (BLW) approach, Mo and co-workers obtained optimized structures and vibrational frequencies of a series of transition metal monocarbonyls with both directions

26

of CT "quenched".[10,79] They revealed that ν_{CO} is uniformly blue-shifted in both neutral and cationic transition metal monocarbonyls when CT is absent, and that CT always results in a red shift in ν_{CO}, which is more pronounced in neutral, classical complexes. The blue shift induced by the transition metal moiety is in line with the Stark effect of CO in an electric field,[74,75] and first arises even without polarization, i.e., on the frozen surface.[45,73] The experimentally observed shift in ν_{CO} is thus a superposition of these effects and the net effect can be small since they induce shifts in opposite directions.

Boron monofluoride is also isoelectronic to CO and N_2, and was predicted to be both a stronger σ-donor and π-acceptor compared against CO.[84–86] It possesses a lower bond order and like CO, the dipole moment of BF is in the opposite direction of intuition, with the B atom as the negative pole.[87,88] However, BF is only stable under extreme conditions, rendering its coordination compounds difficult to prepare.[89,90] Nonetheless, recent work by Drance *et al.* reported the synthesis and characterization of a transition metal complex with a terminal coordinating BF ligand and demonstrated BF's σ-donor and π-acceptor properties.[91] Experimental evidence including NMR-, IR-, and Mössbauer-spectroscopy and X-ray crystallography suggests that BF is not only a stronger σ-donor than its isoelectronic counterparts (CO, N_2) but also a strong π-acceptor. Differing from the analogous complexes with CO and N_2 that exhibit red-shifted ligand stretching frequencies, the B−F stretching frequency, ν_{BF}, is markedly blue-shifted, which is seemingly contradictory to the assignment of BF as a strong π-acceptor.

Using the extended adiabatic ALMO-EDA with the VFB states, one is able to characterize and separate the effects of permanent and induced electrostatics, σ forward donation, and π back-donation on the structural and vibrational properties of a given complex. Here we provide a systematic study of octahedral transition metal complexes with the above-mentioned three isoelectronic ligands: N_2, CO, and BF. In order to compare these three ligands directly, we choose a $[Ru(II)(NH_3)_5]^{2+}$ framework because of its simplicity (homogeneous auxiliary ligands (NH_3) and low-spin singlet state) and its strong association with

π-acidic ligands. Furthermore, the $[\text{Ru(II)}(\text{NH}_3)_5\text{N}_2]^{2+}$ cation is experimentally accessible and has been well characterized.[21]

The vertical ALMO-EDA results at the minimum-energy structure of each complex are summarized in Table 5. Starting with the ammine (NH_3) ligand that is a σ-donor only, we find that it exhibits a favorable frozen interaction due to the large dipole moment of NH_3. It also shows a relatively long Ru$-$N distance (2.2 Å), which gives rise to more favorable electrostatic interaction and weaker Pauli repulsion, respectively. Combined with $\Delta\text{E}_{\text{Pol}}$ (-46 kJ/mol), the total non-CT contribution is significant and constitutes $\sim 30\%$ of the total interaction energy. The CT term, nonetheless, still makes the largest contribution to binding, and is strongly dominated by forward donation ($\text{H}_3\text{N}\rightarrow\text{Ru}$) as indicated by the large CTf/CTb ratio (10.8).

The three π-acidic ligands (N_2, CO, and BF) exhibit drastically different vertical EDA fingerprints than NH_3. Although both permanent electrostatics and polarization become more favorable in these complexes, they are overlaid by the stronger Pauli repulsion that increases from N_2 to BF (see Table S8 in the SI). Thus, CT becomes the key contributor to these interactions. As indicated by the large magnitude of both $\Delta\text{E}_{\text{CTf}}$ and $\Delta\text{E}_{\text{CTb}}$ values, CT in these complexes is of a typical bi-directional character, and the most significant COVPs (Figs. 7 and 8) clearly demonstrate σ forward donation and π back-donation. The total interaction strength of these complexes is in the order of $\text{N}_2 <$ CO $<$ BF, which is also in line with their relative strength of CT. The further decomposition of CT using the VFB approach reveals that N_2 is a much weaker σ-donor as well as a weaker π-acceptor than the more polar CO and BF. The increase in bond polarity ($\text{N}_2 <$ CO $<$ BF) in this isoelectronic series reduces the HOMO-LUMO gap, facilitating both forward and backward donation. The increase in the strength of CT with more polar ligands can also be rationalized with the COVPs shown in Figs. 7 (for N_2) and 8 (for CO and BF), which illustrate that more polar ligands are more favored as either σ-donor or π-acceptor. Interestingly, the relative strength of forward donation increases more rapidly than backward donation with the ligand

Table 5: Vertical ALMO-EDA results for the transition metal complexes. The energies are in kJ/mol and the distance in Å. The ratio refers to $\Delta E_{CTf}/\Delta E_{CTb}$.

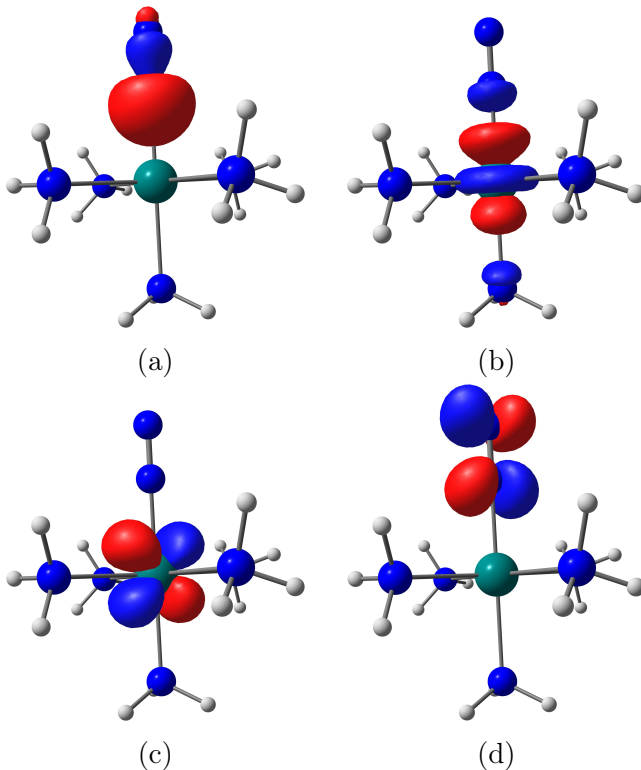| Complex	ΔE_{Frz}	ΔE_{Pol}	ΔE_{CTf}	ΔE_{CTb}	ΔE_{CT}	ΔE_{Tot}	ratio	r(M−X)
$H_3N-[Ru(NH_3)_5]^{2+}$	−11.6	−46.0	−102.4	−9.5	−113.4	−171.0	10.8	2.194
$NN-[Ru(NH_3)_5]^{2+}$	160.4	−70.1	−95.0	−99.5	−212.6	−122.4	1.0	1.951
$OC-[Ru(NH_3)_5]^{2+}$	283.2	−119.6	−190.0	−155.8	−392.8	−229.2	1.2	1.860
$FB-[Ru(NH_3)_5]^{2+}$	317.1	−171.0	−284.8	−130.0	−477.2	−331.1	2.2	1.871
$NN-[Fe(NH_3)_5]^{2+}$	82.4	−57.1	−42.1	−53.2	−100.9	−75.6	0.8	1.929
$NN-[Tc(NH_3)_5]^{+}$	263.8	−75.0	−94.6	−277.4	−414.7	−226.0	0.3	1.873

(a) (b)

(c) (d)

Figure 7: Key COVPs illustrating the σ- and π-type donations in $NN-[Ru(NH_3)_5]^{2+}$: (a) σ-donor, (b) σ-acceptor, (c) π-donor, and (d) π-acceptor.

polarity, as indicated by the increasing CTf/CTb ratio from N_2 to BF. It is also noteworthy that although BF is more polar than CO, which is supposed to yield an even better overlap of π^* with Ru(II)'s 4d orbitals, the back-donation towards BF is 25 kJ/mol less favorable than that towards CO and the interaction between BF and the Ru(II) moiety is dominated by the σ forward donation. These findings hold for different types of density functionals as shown in Table S9 in the SI.
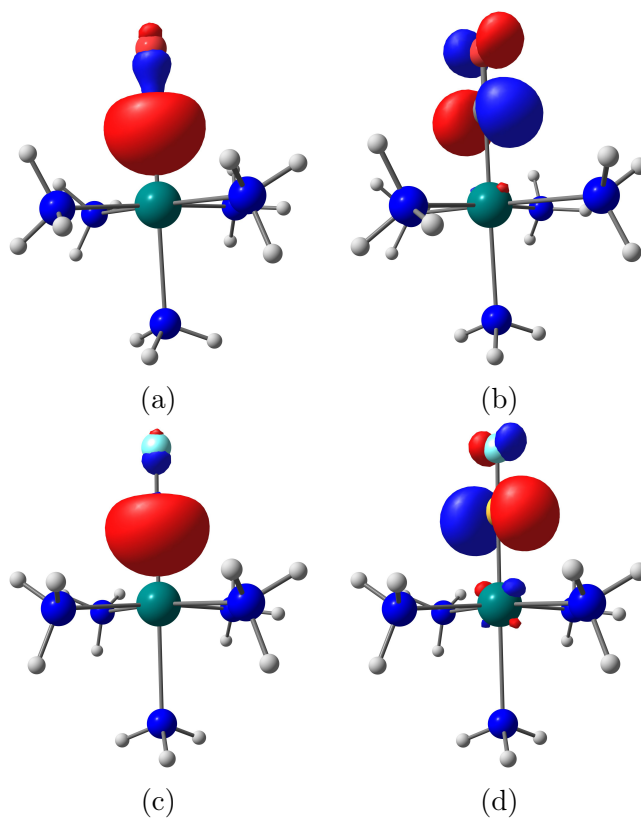
Figure 8: Key COVPs illustrating the σ- and π-type donations in OC$-$[Ru(NH$_3$)$_5$]$^{2+}$: (a) σ-donor, (b) π-acceptor, and in FB$-$[Ru(NH$_3$)$_5$]$^{2+}$: (c) σ-donor, (d) π-acceptor.
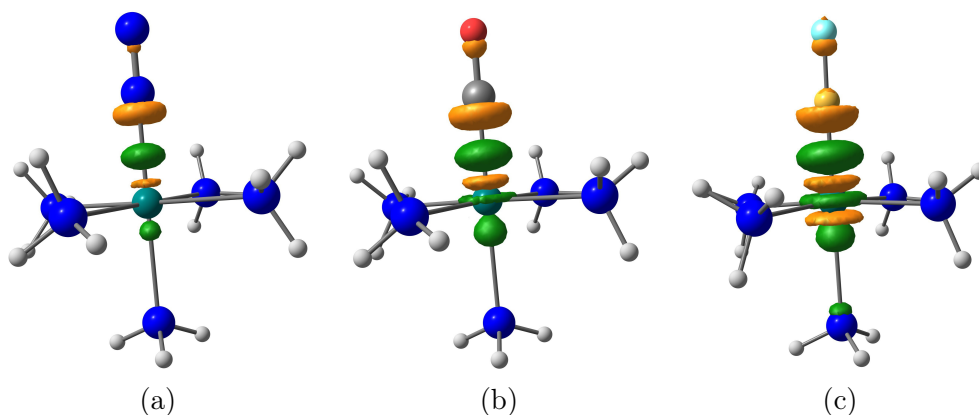

Figure 9: Electron density difference between the CTf and Pol states (plotted with isovalue 0.01 a.u.) for (a) N$_2$$-$[Ru(NH$_3$)$_5$]$^{2+}$, (b) OC$-$[Ru(NH$_3$)$_5$]$^{2+}$, and (c) FB$-$[Ru(NH$_3$)$_5$]$^{2+}$ (green: increase in electron density; yellow: decrease in electron density).

The adiabatic EDA results (Table 6) show that the Ru(II) moiety binds the three π-acidic ligands (denoted as XY) only loosely on the Pol surface with the minimum-energy Ru$-$X distances ranging between 2.6–2.7 Å. This is in contrast to the main group beryllium

carbonyls discussed in Sec. 4.2 above where short intermolecular distances were already observed on the Pol surface (see Table 4). In the case of N_2, introducing either the forward or backward CT shortens the Ru−X distance by ∼0.3 Å, indicating the similar σ-donating and π-accepting abilities of this ligand. For CO, the forward CT shortens the Ru−X distance more than backward CT, and this difference is further enlarged in the case of BF, where forward donation shortens the Ru−X distance by over 0.2 Å. This differs from the two main group examples (OC−BH_3 and OC−BeO) discussed in the above sections, where the adduct bond lengths on the CTb and fully relaxed surfaces are very similar because of the fast decay of CTb energy. For the Ru(II) complexes one can still observe similar fast decay of CTb as shown in Fig. 10. However, the strong Pauli repulsion between the lone pair on the XY ligand and the 4d electrons of Ru(II) do not allow for a shorter Ru−X distance without the presence of forward donation, even though it would greatly increase the strength of back-donation. The forward donation moves electron density from the lone pair of the ligand to Ru(II)'s empty d_{z^2} orbital and thereby reduces the Pauli repulsion, which is illustrated by the COVP acceptor orbital for σ-donation (Fig 7(b)) and the plots of electron density difference between the CTf and Pol states for N_2, CO, and BF (Figs. 9(a)–(c)). Therefore, the forward donation not only stabilizes the complex by itself but also enables stronger back-donation by reducing Pauli repulsion, which allows for a shorter M−X distance. This is not the case in the main group complexes where Pauli repulsion is not as prominent and can already be overcome by the non-CT contributions.

The comparison of the PES scans for these complexes with respect to the Ru−X distance (Fig. 10) further confirms the variation in the relative strength between the forward and backward CT. For the N_2 complex (left panel), CTf and CTb are of similar magnitude over the full range of the r(N−Ru), with CTb being marginally more favorable in the short range and a crossover taking place around 1.9 Å; for the CO complex (middle panel), the CTf surface is consistently of a lower energy than that of CTb although the gap between them is small. The BF ligand (right panel), on the other hand, is an even stronger σ-donor but a
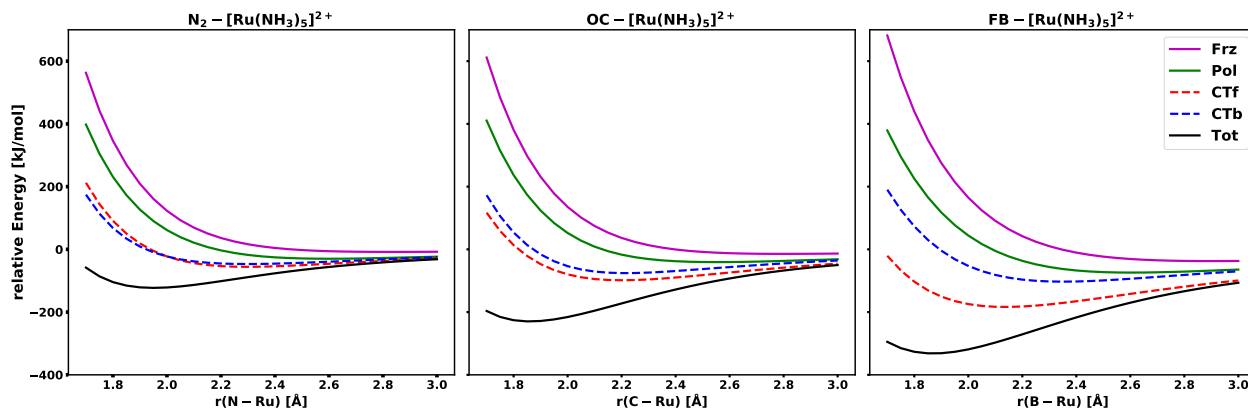
Figure 10: Potential energy surface (rigid scan) for each ALMO-EDA intermediate state (Frz, Pol, CTf, CTb, and Tot) for $N_2-[Ru(NH_3)_5]^{2+}$ (left), $OC-[Ru(NH_3)_5]^{2+}$ (middle), and $FB-[Ru(NH_3)_5]^{2+}$ (right).

weaker π-acceptor, with a substantial gap between the CTf and CTb surfaces. Furthermore, from N_2 to BF the frozen surface becomes less favorable, while the stabilization effect due to of polarization (the difference between Frz and Pol) increases.

Table 6: Metal-ligand distance [r(M−X)] and bond length of the diatomic ligand [r(X−Y)] (both in Å) evaluated on the Pol, CTf, CTb, and Tot surfaces. In the isolated state, r(N−N) = 1.091 Å, r(C−O) = 1.125 Å, r(B−F) = 1.265 Å.

Complex	r(M-X)				r(X-Y)			
	Pol	CTf	CTb	Tot	Pol	CTf	CTb	Tot
$NN-[Ru(NH_3)_5]^{2+}$	2.625	2.308	2.318	1.951	1.090	1.089	1.093	1.104
$OC-[Ru(NH_3)_5]^{2+}$	2.605	2.219	2.329	1.860	1.117	1.114	1.124	1.139
$FB-[Ru(NH_3)_5]^{2+}$	2.690	2.165	2.379	1.871	1.243	1.237	1.249	1.266
$NN-[Fe(NH_3)_5]^{2+}$	2.538	2.267	2.190	1.929	1.090	1.090	1.092	1.097
$NN-[Tc(NH_3)_5]^{+}$	2.638	2.388	2.091	1.873	1.090	1.089	1.115	1.133

The IR shifts in the stretching frequency of these π-acidic ligands (see Table 7) show an opposite trend to the ordering of the strength of their CT energies (ΔE_{CT} in Table 5): a red shift of 150 cm^{-1} for N_2, a smaller red shift of 102 cm^{-1} for CO, and a blue shift of 123 cm^{-1} for BF. The origin of this seemingly counterintuitive trend can be unraveled by the frequency shifts ($\Delta\nu_{XY}$) evaluated on the Pol surface, where the blue shifts increase drastically from N_2 to BF. The blue shift in ν_{XY} for each complex is further increased at the equilibrium structures on the CTf surface, which, as in the $OC-BH_3$ and $OC-BeO$

Table 7: Adiabatic ALMO-EDA results for the shifts in the vibrational frequency of N_2, CO and BF ($\Delta\nu_{XY}$ in cm^{-1}) when associated with the transition metal moieties.

Complex	$\Delta\nu_{XY}$			
	Pol	CTf	CTb	Tot
$NN-[Ru(NH_3)_5]^{2+}$	11	25	−39	−150
$OC-[Ru(NH_3)_5]^{2+}$	74	109	−5	−102
$FB-[Ru(NH_3)_5]^{2+}$	143	208	108	123
$NN-[Fe(NH_3)_5]^{2+}$	7	16	−21	−80
$NN-[Tc(NH_3)_5]^{+}$	16	27	−236	−373

cases, is mainly a geometric effect as indicated by the close agreement between Pol@CTf and CTf@CTf frequencies in Table 8. The backward CT, on the other hand, lowers the frequencies relative to their values on the Pol surface for all three ligands, which, as indicated by the three right columns in Table 8, is truly an electronic effect. For the complex with N_2, the back-donation overpowers the weak electrostatic effect, yielding an overall red-shifted ν_{N_2} on the CTb surface (-39 cm^{-1} relative to the free N_2 stretch). The red shift becomes much more pronounced (-150 cm^{-1} relative to free N_2) when both directions of CT are permitted, which can be explained by the combined effect of forward and backward CT in shortening the Ru−N distance. According to the adiabatic EDA results in Table 6, CTf and CTb shorten the Ru−N distance by 0.32 Å and 0.31 Å, respectively, and when combined they shorten the distance by 0.67 Å, indicating that their effects are almost additive in this case. The shortened Ru−N distance then strengthens both the electrostatic effect (blue-shifting) and the back-donation (red-shifting), whereas the latter plays a dominant role in this case.

The same mechanism applies to both the CO and BF complexes, where the bond shortening effects of CTf and CTb are also nearly additive. However, the relative strength of the blue-shifting electrostatic effect and the red-shifting backward CT, as well as their variation with the Ru−X distance, differs in each complex. The blue shifts on the Pol and CTf surfaces are more significant with more polar ligands, which is in line with the increasingly contracted r(X−Y) from N_2 to BF (see Table 6). The back-bonding to CO appears to exert a strong effect such that the frequency calculated on the CTb surface is red-shifted already

(5 cm^{-1} relative to the free ν_{CO}). The synergy of forward and backward CT further results in a substantial red shift of 102 cm^{-1} in the fully relaxed complex, suggesting that the strength of backward CT increases more rapidly than the blue-shifting electrostatics with the shortening of the Ru$-$C distance. The back-bonding to BF, on the other hand, introduces a less pronounced red shift (35 cm^{-1} relative to ν_{BF} on the Pol surface) such that the frequency evaluated on the CTb surface is still strongly blue-shifted (108 cm^{-1} relative to the free ν_{BF}). More interestingly, with both directions of CT permitted, ν_{BF} becomes more blue-shifted relative to that on the CTb surface, which is opposite to the substantial red shifts induced by the synergistic effect of forward and backward CT found in the N$_2$ and CO complexes, suggesting that the enhancement of the blue-shifting effect overshadows the increase in the strength of back-donation. This is confirmed by the strongly blue-shifted Pol@Tot frequency as shown in Table 9 (314 cm^{-1} relative to the free ν_{BF}), which is 142 cm^{-1} higher than the Pol@CTb frequency. The red shift induced by backward CT, on the other hand, is only increased by 55 cm^{-1} upon moving from the minimum-energy Ru$-$B distance on the CTb surface to that on the fully relaxed surface, and therefore it is overpowered by the enhanced blue-shifting electrostatic effect.

Table 8: Shifts in the stretching frequency of N$_2$, CO, and BF (in cm^{-1}) when associated with [Ru(NH$_3$)$_5$]$^{2+}$ with the Ru$-$X distance fixed at the optimum values on the CTf ("@CTf") and CTb ("@CTb") surfaces, respectively.

Complex	$\Delta\nu_{XY}$@CTf			$\Delta\nu_{XY}$@CTb		
	Pol	CTf	$\Delta\nu_{CTf}$	Pol	CTb	$\Delta\nu_{CTb}$
NN$-$[Ru(NH$_3$)$_5$]$^{2+}$	33	25	-8	32	-39	-71
OC$-$[Ru(NH$_3$)$_5$]$^{2+}$	107	109	2	92	-5	-97
FB$-$[Ru(NH$_3$)$_5$]$^{2+}$	207	208	1	172	108	-64

We then perform the same set of analyses on NN$-$[Fe(NH$_3$)$_5$]$^{2+}$, which is the 3d analogue of the Ru(II)$-$N$_2$ complex. The 3d electrons are more compact than 4d, resulting in an almost halved magnitude of the ΔE_{Frz} and ΔE_{CT} terms at the equilibrium structure compared to the values of the corresponding Ru(II) complex (see Table 5). Turning to the

Table 9: Shifts in the stretching frequency of N_2, CO, and BF (in cm^{-1}) when associated with $[Ru(NH_3)_5]^{2+}$ evaluated at the fully relaxed minimum-energy Ru$-$X distance ("@Tot").

| | $\Delta\nu_{XY}$@Tot | | | |
Complex	Pol	CTf	CTb	Tot
NN$-[Ru(NH_3)_5]^{2+}$	105	83	-73	-150
OC$-[Ru(NH_3)_5]^{2+}$	217	188	7	-103
FB$-[Ru(NH_3)_5]^{2+}$	314	305	195	123

adiabatic EDA results (Table 6), the Fe$-$N distance optimized in the Pol state is $\sim$0.1 Å shorter than the corresponding Ru$-$N distance, which is consistent with the weaker Pauli repulsion exerted by the 3d orbitals. Nonetheless, once fully relaxed, r(Fe$-$N) is only $\sim$0.02 Å shorter than r(Ru$-$N) optimized in the same state, indicating the stronger effects of CT in the Ru(II) complex. One should also note that the forward CT has a weaker effect than backward CT on the Fe(II) complex, which is revealed by its CTf/CTb ratio (0.8) as well as the significantly larger Fe$-$N distance on the CTf surface than on CTb. The decomposition of the shift in ν_{N2} follows the synergistic mechanism discussed above, whereas the overall red shift (relative to the free ν_{N2}) for the Fe(II) complex is slightly more than one half of that for the Ru(II) complex, which is consistent with the relative strength of their ΔE_{CTb} values in Table 5.

At last we investigate the Tc(I) complex with N_2, where the metal center is also of $4d^6$ configuration but has a different oxidation state. Compared to the Ru(II) complex, the frozen interaction at the equilibrium geometry is over 100 kJ/mol more repulsive (Table 5) due to the more diffuse d-orbitals of Tc(I), while their ΔE_{Pol} and ΔE_{CTf} terms only minimally differ. The backward CT, however, almost *triples* upon the replacement of Ru(II) with Tc(I), resulting in an overall CT stabilization energy that is over 200 kJ/mol more favorable in the latter. The results of adiabatic EDA further highlight the prominent contribution from back-donation in the Tc(I) complex, such as the significant elongation of the N$-$N bond (Table 6) and the substantial red shift in ν_{NN} (236 cm^{-1} relative the free N_2) that already appears on the CTb surface (Table 7). Despite the overwhelming dominance of CTb, the Tc$-$N distance

on the CTb surface is still over 0.2 Å longer than the fully relaxed equilibrium distance. This demonstrates that even for strong π-donating metals, CTf still plays an important role in overcoming the Pauli repulsion to achieve the final metal-ligand distance. Surprisingly, the Ru(II) and Tc(I) complexes show similar N$-$N bond lengths and frequency blue shifts on the Pol and CTf surfaces. A closer look at the structures of these complexes reveals that the M$-$NH$_3$ distances are almost 0.1 Å shorter in the Ru(II) complex, indicating the stronger donation from the ammine ligands to Ru^{2+} that partially neutralizes its excessive positive charges. Finally, we note that the synergistic effect of forward and backward CT remains significant for the Tc(I) complex despite the dominance of backward CT, which is indicated by the further elongated r(N$-$N) and more red-shifted ν_{N_2} when both directions of CT are permitted.

5   Conclusions

Making use of the flexibility of the generalized SCF-MI scheme, we introduced two new intermediate states in which only one direction of CT is permitted under the ALMO-EDA framework. This allows us to separate a total CT stabilization energy into forward (CTf) and backward (CTb) contributions with a residual higher-order term. This new variational forward-backward (VFB) decomposition scheme yields similar results compared to the previously developed ALMO-CTA that employs a perturbative approach. An important difference is that, these two new intermediate states are each variationally optimized such that their energies are strict variational upper bounds to the full SCF energy and the nuclear forces associated with them can thus be readily computed, rendering it possible for one to identify the forward and backward CT contributions to the changes in structural and vibrational properties upon the formation of dative complexes.

As a proof-of-concept example, we first applied VFB analysis to the OC$-$BH$_3$ complex. The decomposition of ΔE_{CT} reveals that while CTf and CTb are of similar strength at

the minimum-energy distance, the backward donation from BH_3 to CO decays substantially faster in the long range. This steep distance dependence of the strength of back-donation, together with the relatively weak Pauli repulsion due to the electron-deficient nature of BH_3, elucidates the close agreement between the minimum-energy C−B distances on the CTb and Tot surfaces. The CO stretching frequency (ν_{CO}) in this system is only minimally shifted relative to that of the free CO, and the adiabatic ALMO-EDA results show that ν_{CO} is strongly blue-shifted on the CTf surface and moderately blue-shifted on the CTb surface, which are seemingly counterintuitive. We identified the significant blue-shifting effect of the electrostatic interaction as it shrinks the CO bond distance to increase the dipole moment of CO, which is further enhanced upon the shortening of the C−B distance driven by CT. This blue-shifting electrostatic effect largely cancels out the red-shifting effect of the back-donation.

We then applied VFB analysis to the carbonyl complexes of BeY (Y = O or CO_3), where CO is bound to the BeY moiety under either the κC or κO mode. At their equilibrium structures, the κC complexes are more strongly bound than their respective κO isomers, and the energy differences are rather evenly distributed betwee the Frz, Pol, and CTb terms. The CO stretching frequencies in the κC and κO complexes are blue- and red-shifted, respectively, which agree with the results in Ref. 76. Using the adiabatic ALMO-EDA, we demonstrated that the opposite shifts in ν_{CO} originate from the frozen interaction, which can be attributed to the molecular Stark effect: depending on the orientation of the CO dipole to the Lewis acid, the electrostatic interaction induces a blue shift (κC) or a red shift (κO). Both Pol and CTb further increases the blue/red shift in the κC/κO complexes simply by shortening the intermolecular distances. The backward CT red-shifts ν_{CO} in both the κC and κO complexes and has a stronger effect in the former because of the larger amplitude of the π^* orbital on the C atom. Nevertheless, the backward CT is not of enough strength to overcome the blue-shifting electrostatics in the κC isomers, especially in the case of OC−$BeCO_3$ where the back-donation is particularly weak. The sizable red shifts in the κO complexes, on the other

hand, result from the cooperation of the electrostatic effect and backward CT in elongating and weakening the O$-$C bond.

Finally we investigated the complexes of N$_2$, CO, and BF with the $[\text{Ru(II)(NH}_3)_5]^{2+}$ moiety. The vertical EDA results at the minimum-energy structures reveal that the total binding strength increases in the order of N$_2$ < CO < BF, which is attributed to the enhanced Pol and CT terms that overshadow increased Pauli repulsion. The adiabatic VFB-EDA results show that the contributions from CTf and CTb to the shortening of the Ru$-$X distance are almost additive, which differs from the scenarios of the complexes with main group Lewis acids (BH$_3$, BeO/BeCO$_3$) where intermolecular distance obtained on the CTb surface is already close to the full equilibrium distance. This result can be rationalized by stronger Pauli repulsion exerted by the d-electrons of the transition metal center, whose alleviation requires the assistance of forward CT. A counterintuitive trend is observed for the shifts in the stretching frequency of these ligands, with both ν_{N_2} and ν_{CO} red-shifted (-150 and -102 cm^{-1}, respectively) and ν_{BF} strongly blue-shifted ($+123$ cm^{-1}), which is not consistent with their relative strength of ΔE_{CTb}. Our further decomposition of the frequency shifts demonstrated that the molecular Stark effect induces a stronger blue shift for a more polar π-acidic ligand, and its enhancement with the decrease of the Ru$-$X distance exceeds the red shift due to π back-donation, giving rise to the unusual blue shift in ν_{BF}.

In summary, our new VFB extension of the ALMO-EDA provides a useful tool to characterize the roles played by forward and backward CT in the formation of dative complexes, which complements the currently available ALMO-CTA scheme by allowing the decomposition of shifts in molecular properties. The application of VFB analysis to main group and transition metal complexes with π-acidic ligands further revealed that permanent electrostatics and π back-donation are the two crucial parameters in determining the shifts in vibrational frequencies ($\Delta\nu_{\text{XY}}$). Our results highlighted that $\Delta\nu_{\text{XY}}$ may become an unreliable metric for the strength of π back-donation because of the often pronounced electrostatic effect in the bonding regime.

Acknowledgement

Supporting Information Available

Replication of the main findings with both B97-D and ωB97X-D; decomposition of the frozen interaction energy into electrostatic, Pauli repulsion, and dispersion for all three examples studied; comparison of the results given by perturbative ALMO-CTA and the decomposition scheme presented in this work; COVPs and electron density difference plots illustrating the interaction between BH_3 and $BeO/BeCO_3$ with CO; comparison of the decay rate of ΔE_{CTf} for the κC and κO isomers of BeO; PES for each ALMO-EDA intermediate state for $H_3N-[Ru(NH_3)_5]^{2+}$;

References

(1) Miessler, G.; Fischer, P.; Tarr, D. *Inorganic Chemistry*, 5th ed.; Pearson Education, 2014.

(2) Dewar, J. A review of the pi-complex theory. *Bull. Soc. Chim. Fr.* **1951**, *18*, C71–C79.

(3) Chatt, J.; Duncanson, L. A. 586. Olefin co-ordination compounds. Part III. Infra-red spectra and structure: attempted preparation of acetylene complexes. *J. Chem. Soc.* **1953**, 2939–2947.

(4) Elian, M.; Hoffmann, R. Bonding capabilities of transition metal carbonyl fragments. *Inorg. Chem* **1975**, *14*, 1058–1076.

(5) Ziegler, T.; Rauk, A. Carbon monoxide, carbon monosulfide, molecular nitrogen, phosphorus trifluoride, and methyl isocyanide as. sigma. donors and. pi. acceptors. A theoretical study by the Hartree-Fock-Slater transition-state method. *Inorg. Chem* **1979**, *18*, 1755–1759.

(6) Dapprich, S.; Frenking, G. Investigation of donor-acceptor interactions: A charge decomposition analysis using fragment molecular orbitals. *J. Phys. Chem.* **1995**, *99*, 9352–9362.

(7) Ehlers, A. W.; Dapprich, S.; Vyboishchikov, S. F.; Frenking, G. Structure and Bonding of the Transition-Metal Carbonyl Complexes $M(CO)_5L$ (M= Cr, Mo, W) and $M(CO)_3L$ (M= Ni, Pd, Pt; L= CO, SiO, CS, N_2, NO^+, CN^-, NC^-, HCCH, CCH_2, CH_2, CF_2, H_2). *Organometallics* **1996**, *15*, 105–117.

(8) Matito, E.; Solà, M. The role of electronic delocalization in transition metal complexes from the electron localization function and the quantum theory of atoms in molecules viewpoints. *Coord. Chem. Rev.* **2009**, *253*, 647–665.

(9) Khaliullin, R. Z.; Bell, A. T.; Head-Gordon, M. Analysis of charge transfer effects in molecular complexes based on absolutely localized molecular orbitals. *J. Chem. Phys* **2008**, *128*, 184112.

(10) Mo, Y.; Bao, P.; Gao, J. Energy decomposition analysis based on a block-localized wavefunction and multistate density functional theory. *Phys. Chem. Chem. Phys.* **2011**, *13*, 6760–6775.

(11) Mond, L.; Langer, C.; Quincke, F. L.–Action of carbon monoxide on nickel. *J. Chem. Soc., Trans.* **1890**, *57*, 749–753.

(12) Cotton, F. Metal carbonyls: some new observations in an old field. *Progr. Inorg. Chem* **1976**, *21*, 1–28.

(13) Herrmann, W. A. 100 years of metal carbonyls: a serendipitous chemical discovery of major scientific and industrial impact. *J. Organomet. Chem.* **1990**, *383*, 21–44.

(14) Lin, J. T.; Hagen, G. P.; Ellis, J. E. Highly reduced organometallics. 9. Synthesis and characterization of the tetrasodium tetracarbonylmetalates(4-) of chromium, molybdenum, and tungsten, $Na_4M(CO)_4$: their reactions with weak acids to generate $H_2M_2(CO)_8^{2-}$ (M = Cr, Mo, and W). *J. Am. Chem. Soc.* **1983**, *105*, 2296–2303.

(15) Lupinetti, A. J.; Strauss, S. H.; Frenking, G. *Progress in Inorganic Chemistry*; John Wiley & Sons, Ltd, 2007; pp 1–112.

(16) Bauschlicher, C. W.; Ricca, A. On the interaction of CO and NH_3 with BH_3 and BF_3. *Chem. Phys. Lett* **1995**, *237*, 14–19.

(17) Khaliullin, R. Z.; Cobar, E. A.; Lochan, R. C.; Bell, A. T.; Head-Gordon, M. Unravelling the Origin of Intermolecular Interactions Using Absolutely Localized Molecular Orbitals. *J. Phys. Chem. A* **2007**, *111*, 8753–8765.

(18) Stephan, D. W.; Erker, G. Frustrated Lewis pair chemistry of carbon, nitrogen and sulfur oxides. *Chem. Sci.* **2014**, *5*, 2625–2641.

(19) Wu, X.; Zhao, L.; Jin, J.; Pan, S.; Li, W.; Jin, X.; Wang, G.; Zhou, M.; Frenking, G. Observation of alkaline earth complexes $M(CO)_8$ (M= Ca, Sr, or Ba) that mimic transition metals. *Science* **2018**, *361*, 912–916.

(20) Wu, X.; Zhao, L.; Jiang, D.; Fernández, I.; Berger, R.; Zhou, M.; Frenking, G. Barium as honorary transition metal in action: Experimental and theoretical study of $Ba(CO)^+$ and $Ba(CO)^-$. *Angew. Chem. Int. Ed.* **2018**, *57*, 3974–3980.

(21) Allen, A. D.; Senoff, C. V. Nitrogenopentammineruthenium(II) complexes. *Chem. Commun.* **1965**, 621–622.

(22) Bazhenova, T.; Shilov, A. Nitrogen fixation in solution. *Coord. Chem. Rev.* **1995**, *144*, 69–145.

(23) MacKay, B. A.; Fryzuk, M. D. Dinitrogen Coordination Chemistry: On the Biomimetic Borderlands. *Chem. Rev.* **2004**, *104*, 385–402.

(24) Laplaza, C. E.; Cummins, C. C. Dinitrogen Cleavage by a Three-Coordinate Molybdenum(III) Complex. *Science* **1995**, *268*, 861–863.

(25) Yandulov, D. V.; Schrock, R. R. Catalytic Reduction of Dinitrogen to Ammonia at a Single Molybdenum Center. *Science* **2003**, *301*, 76–78.

(26) Tanabe, Y.; Nishibayashi, Y. Developing more sustainable processes for ammonia synthesis. *Coord. Chem. Rev.* **2013**, *257*, 2551–2564.

(27) Anderson, J. S.; Rittle, J.; Peters, J. C. Catalytic conversion of nitrogen to ammonia by an iron model complex. *Nature* **2013**, *501*, 84–87.

(28) MacLeod, K. C.; Holland, P. L. Recent developments in the homogeneous reduction of dinitrogen by molybdenum and iron. *Nat. Chem.* **2013**, *5*, 559–565.

(29) Fajardo, J.; Peters, J. C. Catalytic Nitrogen-to-Ammonia Conversion by Osmium and Ruthenium Complexes. *J. Am. Chem. Soc.* **2017**, *139*, 16105–16108.

(30) Foster, S. L.; Bakovic, S. I. P.; Duda, R. D.; Maheshwari, S.; Milton, R. D.; Minteer, S. D.; Janik, M. J.; Renner, J. N.; Greenlee, L. F. Catalysts for nitrogen reduction to ammonia. *Nat. Catal.* **2018**, *1*, 490–500.

(31) Chen, J. G.; Crooks, R. M.; Seefeldt, L. C.; Bren, K. L.; Bullock, R. M.; Darensbourg, M. Y.; Holland, P. L.; Hoffman, B.; Janik, M. J.; Jones, A. K.; Kanatzidis, M. G.; King, P.; Lancaster, K. M.; Lymar, S. V.; Pfromm, P.; Schneider, W. F.; Schrock, R. R. Beyond fossil fuel–driven nitrogen transformations. *Science* **2018**, *360*.

(32) Phipps, M. J.; Fox, T.; Tautermann, C. S.; Skylaris, C.-K. Energy decomposition analysis approaches and their evaluation on prototypical protein–drug interaction patterns. *Chem. Soc. Rev.* **2015**, *44*, 3177–3211.

(33) Pastorczak, E.; Corminboeuf, C. Perspective: Found in translation: Quantum chemical tools for grasping non-covalent interactions. *J. Chem. Phys.* **2017**, *146*, 120901.

(34) Zhao, L.; von Hopffgarten, M.; Andrada, D. M.; Frenking, G. Energy decomposition analysis. *WIREs: Comput. Mol. Sci.* **2018**, *8*, e1345.

(35) Kitaura, K.; Morokuma, K. A new energy decomposition scheme for molecular interactions within the Hartree-Fock approximation. *Int. J. Quantum Chem.* **1976**, *10*, 325–340.

(36) Morokuma, K. Why do molecules interact? The origin of electron donor-acceptor complexes, hydrogen bonding and proton affinity. *Acc. Chem. Res.* **1977**, *10*, 294–300.

(37) Stevens, W. J.; Fink, W. H. Frozen fragment reduced variational space analysis of hydrogen bonding interactions. Application to the water dimer. *Chem. Phys. Lett.* **1987**, *139*, 15–22.

(38) Bagus, P. S.; Hermann, K.; Bauschlicher Jr, C. W. A new analysis of charge transfer and polarization for ligand–metal bonding: Model studies of Al_4CO and Al_4NH_3. *J. Chem. Phys.* **1984**, *80*, 4378–4386.

(39) Reed, A. E.; Weinhold, F. Natural bond orbital analysis of near-Hartree–Fock water dimer. *J. Chem. Phys.* **1983**, *78*, 4066–4073.

(40) Reed, A. E.; Curtiss, L. A.; Weinhold, F. Intermolecular interactions from a natural bond orbital, donor-acceptor viewpoint. *Chem. Rev.* **1988**, *88*, 899–926.

(41) Khaliullin, R. Z.; Head-Gordon, M.; Bell, A. T. An efficient self-consistent field method for large systems of weakly interacting components. *J. Chem. Phys* **2006**, *124*, 204105.

(42) Liang, W.; Head-Gordon, M. An exact reformulation of the diagonalization step in electronic structure calculations as a set of second order nonlinear equations. *J. Chem. Phys.* **2004**, *120*, 10379–10384.

(43) Mao, Y.; Horn, P. R.; Head-Gordon, M. Energy decomposition analysis in an adiabatic picture. *Phys. Chem. Chem. Phys.* **2017**, *19*, 5944–5958.

(44) Ramos-Cordoba, E.; Lambrecht, D. S.; Head-Gordon, M. Charge-transfer and the hydrogen bond: Spectroscopic and structural implications from electronic structure calculations. *Faraday Discuss.* **2011**, *150*, 345–362.

(45) Mao, Y.; Ge, Q.; Horn, P. R.; Head-Gordon, M. On the Computational Characterization of Charge-Transfer Effects in Noncovalently Bound Molecular Complexes. *J. Chem. Theory Comput.* **2018**, *14*, 2401–2417.

(46) Ang, S. J.; Mak, A. M.; Wong, M. W. Nature of halogen bonding involving systems, nitroxide radicals and carbenes: a highlight of the importance of charge transfer. *Phys. Chem. Chem. Phys.* **2018**, *20*, 26463–26478.

(47) Thirman, J.; Engelage, E.; Huber, S. M.; Head-Gordon, M. Characterizing the interplay of Pauli repulsion, electrostatics, dispersion and charge transfer in halogen bonding with energy decomposition analysis. *Phys. Chem. Chem. Phys.* **2018**, *20*, 905–915.

(48) Mao, Y.; Head-Gordon, M. Probing Blue-Shifting Hydrogen Bonds with Adiabatic Energy Decomposition Analysis. *J. Phys. Chem. Lett.* **2019**, *10*, 3899–3905.

(49) Bagus, P. S.; Hermann, K.; Bauschlicher Jr, C. W. On the nature of the bonding of lone pair ligands to a transition metal. *J. Chem. Phys.* **1984**, *81*, 1966–1974.

(50) Bauschlicher Jr, C. W.; Bagus, P. S.; Nelin, C. J.; Roos, B. O. The nature of the bonding in XCO for X= Fe, Ni, and Cu. *J. Chem. Phys.* **1986**, *85*, 354–364.

(51) Berquist, E.; Lambrecht, D. A First Principles Approach for Partitioning Linear Response Properties into Additive and Cooperative Contributions. 10.26434/chemrxiv.5773968.v1.

(52) Lambrecht, D. S. Generalizing energy decomposition analysis to response properties to inform expedited predictive models. *Comput. Theor. Chem.* **2019**, *1149*, 24–30.

(53) Horn, P. R.; Mao, Y.; Head-Gordon, M. Probing non-covalent interactions with a second generation energy decomposition analysis using absolutely localized molecular orbitals. *Phys. Chem. Chem. Phys.* **2016**, *18*, 23067–23079.

(54) Horn, P. R.; Mao, Y.; Head-Gordon, M. Defining the contributions of permanent electrostatics, Pauli repulsion, and dispersion in density functional theory calculations of intermolecular interaction energies. *J. Chem. Phys.* **2016**, *144*, 114107.

(55) Mao, Y.; Demerdash, O.; Head-Gordon, M.; Head-Gordon, T. Assessing ion-water interactions in the AMOEBA force field using energy decomposition analysis of electronic structure calculations. *J. Chem. Theory Comput.* **2016**, *12*, 5422–5437.

(56) Stoll, H.; Wagenblast, G.; Preuβ, H. On the use of local basis sets for localized molecular orbitals. *Theor. Chem. Acc.* **1980**, *57*, 169–178.

(57) Gianinetti, E.; Raimondi, M.; Tornaghi, E. Modification of the Roothaan equations to exclude BSSE from molecular interaction calculations. *Int. J. Quantum Chem.* **1996**, *60*, 157–166.

(58) Horn, P. R.; Head-Gordon, M. Polarization contributions to intermolecular interactions revisited with fragment electric-field response functions. *J. Chem. Phys.* **2015**, *143*, 114111.

(59) Löwdin, P.-O. *Advances in quantum chemistry*; Elsevier, 1970; Vol. 5; pp 185–199.

(60) Shao, Y.; Gan, Z.; Epifanovsky, E.; Gilbert, A. T.; Wormit, M.; Kussmann, J.; Lange, A. W.; Behn, A.; Deng, J.; Feng, X.; Ghosh, D.; Goldey, M.; Horn, P. R.; Jacobson, L. D.; Kaliman, I.; Khaliullin, R. Z.; KuÅŻ, T.; Landau, A.; Liu, J.; Proynov, E. I.; Rhee, Y. M.; Richard, R. M.; Rohrdanz, M. A.; Steele, R. P.; Sundstrom, E. J.; III, H. L. W.; Zimmerman, P. M.; Zuev, D.; Albrecht, B.; Alguire, E.; Austin, B.; Beran, G. J. O.; Bernard, Y. A.; Berquist, E.; Brandhorst, K.; Bravaya, K. B.; Brown, S. T.; Casanova, D.; Chang, C.-M.; Chen, Y.; Chien, S. H.; Closser, K. D.; Crittenden, D. L.; Diedenhofen, M.; Jr., R. A. D.; Do, H.; Dutoi, A. D.; Edgar, R. G.; Fatehi, S.; Fusti-Molnar, L.; Ghysels, A.; Golubeva-Zadorozhnaya, A.; Gomes, J.; Hanson-Heine, M. W.; Harbach, P. H.; Hauser, A. W.; Hohenstein, E. G.; Holden, Z. C.; Jagau, T.-C.; Ji, H.; Kaduk, B.; Khistyaev, K.; Kim, J.; Kim, J.; King, R. A.; Klunzinger, P.; Kosenkov, D.; Kowalczyk, T.; Krauter, C. M.; Lao, K. U.; Laurent, A. D.; Lawler, K. V.; Levchenko, S. V.; Lin, C. Y.; Liu, F.; Livshits, E.; Lochan, R. C.; Luenser, A.; Manohar, P.; Manzer, S. F.; Mao, S.-P.; Mardirossian, N.; Marenich, A. V.; Maurer, S. A.; Mayhall, N. J.; Neuscamman, E.; Oana, C. M.; Olivares-Amaya, R.; OâĂŹNeill, D. P.; Parkhill, J. A.; Perrine, T. M.; Peverati, R.; Prociuk, A.; Rehn, D. R.; Rosta, E.; Russ, N. J.; Sharada, S. M.; Sharma, S.; Small, D. W.; Sodt, A.; Stein, T.; StÃijck, D.; Su, Y.-C.; Thom, A. J.; Tsuchimochi, T.; Vanovschi, V.; Vogt, L.; Vydrov, O.; Wang, T.; Watson, M. A.; Wenzel, J.; White, A.; Williams, C. F.; Yang, J.; Yeganeh, S.; Yost, S. R.; You, Z.-Q.; Zhang, I. Y.; Zhang, X.; Zhao, Y.; Brooks, B. R.; Chan, G. K.; Chipman, D. M.; Cramer, C. J.; III, W. A. G.; Gordon, M. S.; Hehre, W. J.; Klamt, A.; III, H. F. S.; Schmidt, M. W.; Sherrill, C. D.; Truhlar, D. G.; Warshel, A.; Xu, X.; Aspuru-Guzik, A.; Baer, R.; Bell, A. T.; Besley, N. A.; Chai, J.-D.; Dreuw, A.; Dunietz, B. D.; Furlani, T. R.; Gwaltney, S. R.; Hsu, C.-P.; Jung, Y.; Kong, J.; Lambrecht, D. S.; Liang, W.; Ochsenfeld, C.; Rassolov, V. A.; Slipchenko, L. V.; Subotnik, J. E.; Voorhis, T. V.; Herbert, J. M.; Krylov, A. I.; Gill, P. M.; Head-Gordon, M. Advances in molecular quantum chemistry contained in

the Q-Chem 4 program package. *Mol. Phys.* **2015**, *113*, 184–215.

(61) Becke, A. D. Density-functional exchange-energy approximation with correct asymptotic behavior. *Phys. Rev. A* **1988**, *38*, 3098.

(62) Lee, C.; Yang, W.; Parr, R. G. Development of the Colle-Salvetti correlation-energy formula into a functional of the electron density. *Phys. Rev. B* **1988**, *37*, 785.

(63) Becke, A. D. Density-functional thermochemistry. III. The role of exact exchange. *J. Chem. Phys.* **1993**, *98*, 5648–5652.

(64) Rappoport, D.; Furche, F. Property-optimized Gaussian basis sets for molecular response calculations. *J. Chem. Phys.* **2010**, *133*, 134105.

(65) Peterson, K. A.; Figgen, D.; Goll, E.; Stoll, H.; Dolg, M. Systematically convergent basis sets with relativistic pseudopotentials. II. Small-core pseudopotentials and correlation consistent basis sets for the post-d group 16-18 elements. *J. Chem. Phys.* **2003**, *119*, 11113–11123.

(66) Mardirossian, N.; Head-Gordon, M. Thirty years of density functional theory in computational chemistry: an overview and extensive assessment of 200 density functionals. *Mol. Phys.* **2017**, *115*, 2315–2372.

(67) Grimme, S. Semiempirical GGA-type density functional constructed with a long-range dispersion correction. *J. Comput. Chem.* **2006**, *27*, 1787–1799.

(68) Chai, J.-D.; Head-Gordon, M. Long-range corrected hybrid density functionals with damped atom-atom dispersion corrections. *Phys. Chem. Chem. Phys.* **2008**, *10*, 6615–6620.

(69) Hait, D.; Head-Gordon, M. Delocalization Errors in Density Functional Theory Are Essentially Quadratic in Fractional Occupation Number. *J. Phys. Chem. Lett.* **2018**, *9*, 6280–6288.

(70) Gordy, W.; Ring, H.; Burg, A. B. Microwave Determination of the Structure of Borine Carbonyl and of the Nuclear Moments of the Stable Boron Isotopes. *Phys. Rev.* **1950**, *78*, 512–517.

(71) Bethke, G. W.; Wilson, M. K. Vibrational Spectrum of Borine Carbonyl. *J. Chem. Phys.* **1957**, *26*, 1118–1130.

(72) Jacobsen, H.; Berke, H.; Döring, S.; Kehr, G.; Erker, G.; Fröhlich, R.; Meyer, O. Lewis Acid Properties of Tris(pentafluorophenyl)borane. Structure and Bonding in L–$B(C_6F_5)_3$ Complexes. *Organometallics* **1999**, *18*, 1724–1735.

(73) Rossomme, E. C.; Lininger, C. N.; Bell, A. T.; Head-Gordon, T.; Head-Gordon, M. Electronic structure calculations permit identification of the driving forces behind frequency shifts in transition metal monocarbonyls. *Phys. Chem. Chem. Phys.* **2020**, *22*, 781–798.

(74) Goldman, A. S.; Krogh-Jespersen, K. Why Do Cationic Carbon Monoxide Complexes Have High C- O Stretching Force Constants and Short C- O Bonds? Electrostatic Effects, Not σ-Bonding. *J. Am. Chem. Soc.* **1996**, *118*, 12159–12166.

(75) Lupinetti, A. J.; Fau, S.; Frenking, G.; Strauss, S. H. Theoretical Analysis of the Bonding between CO and Positively Charged Atoms. *J. Phys. Chem. A* **1997**, *101*, 9551–9559.

(76) Chen, M.; Zhang, Q.; Zhou, M.; Andrada, D. M.; Frenking, G. Carbon Monoxide Bonding With BeO and $BeCO_3$: Surprisingly High CO Stretching Frequency of $OCBeCO_3$. *Angew. Chem. Int. Ed.* **2015**, *54*, 124–128.

(77) Thompson, C. A.; Andrews, L. Noble Gas Complexes with BeO: Infrared Spectra of NG-BeO (NG = Ar, Kr, Xe). *J. Am. Chem. Soc.* **1994**, *116*, 423–424.

(78) Mitoraj, M. P.; Michalak, A.; Ziegler, T. A Combined Charge and Energy Decomposition Scheme for Bond Analysis. *J. Chem. Theory Comput.* **2009**, *5*, 962–975.

(79) Nakashima, K.; Zhang, X.; Xiang, M.; Lin, Y.; Lin, M.; Mo, Y. Block-localized wavefunction energy decomposition (BLW-ED) analysis of σ/π interactions in metal-carbonyl bonding. *J. Theory Comput. Chem.* **2008**, *7*, 639–654.

(80) Bistoni, G.; Rampino, S.; Scafuri, N.; Ciancaleoni, G.; Zuccaccia, D.; Belpassi, L.; Tarantelli, F. How π back-donation quantitatively controls the CO stretching response in classical and non-classical metal carbonyl complexes. *Chem. Sci.* **2016**, *7*, 1174–1184.

(81) Frenking, G.; Loschen, C.; Krapp, A.; Fau, S.; Strauss, S. H. Electronic structure of CO–an exercise in modern chemical bonding theory. *J. Comput. Chem.* **2007**, *28*, 117–126.

(82) Belpassi, L.; Infante, I.; Tarantelli, F.; Visscher, L. The chemical bond between Au (I) and the noble gases. Comparative study of NgAuF and NgAu$^+$ (Ng= Ar, Kr, Xe) by density functional and coupled cluster methods. *J. Am. Chem. Soc.* **2008**, *130*, 1048–1060.

(83) Bistoni, G.; Belpassi, L.; Tarantelli, F. Advances in Charge Displacement Analysis. *J. Chem. Theory Comput.* **2016**, *12*, 1236–1244.

(84) Radius, U.; Bickelhaupt, F. M.; Ehlers, A. W.; Goldberg, N.; Hoffmann, R. Is CO a special ligand in organometallic chemistry? Theoretical investigation of AB, Fe(CO)$_4$AB, and Fe(AB)$_5$ (AB= N$_2$, CO, BF, SiO). *Inorg. Chem* **1998**, *37*, 1080–1090.

(85) Ehlers, A. W.; Baerends, E. J.; Bickelhaupt, F. M.; Radius, U. Alternatives to the CO Ligand: Coordination of the Isolobal Analogues BF, BNH$_2$, BN(CH$_3$)$_2$, and BO- in Mono- and Binuclear First-Row Transition Metal Complexes. *Chem.: Eur. J.* **1998**, *4*, 210–221.

(86) Xu, L.; Li, Q.-S.; Xie, Y.; King, R. B.; Schaefer, H. F. Prospects for Making Organometallic Compounds with BF Ligands: Fluoroborylene Iron Carbonyls. *Inorg. Chem.* **2010**, *49*, 1046–1055.

(87) Fantuzzi, F.; Cardozo, T. M.; Nascimento, M. A. C. Nature of the chemical bond and origin of the inverted dipole moment in boron fluoride: A generalized valence bond approach. *J. Phys. Chem. A* **2015**, *119*, 5335–5343.

(88) Zhao, L.; Hermann, M.; Schwarz, W. E.; Frenking, G. The Lewis electron-pair bonding model: modern energy decomposition analysis. *Nat. Rev. Chem.* **2019**, *3*, 48–63.

(89) Timms, P. Boron-fluorine chemistry. I. Boron monofluoride and some derivatives. *J. Am. Chem. Soc.* **1967**, *89*, 1629–1632.

(90) Timms, P. Boron-fluorine chemistry. II. Reaction of boron monofluoride with acetylenes. *J. Am. Chem. Soc.* **1968**, *90*, 4585–4589.

(91) Drance, M. J.; Sears, J. D.; Mrse, A. M.; Moore, C. E.; Rheingold, A. L.; Neidig, M. L.; Figueroa, J. S. Terminal coordination of diatomic boron monofluoride to iron. *Science* **2019**, *363*, 1203–1205.

Graphical TOC Entry